

Is the mm/sub-mm dust polarization a robust tracer of the magnetic field topology in protostellar envelopes ? A model exploration

Valeska Valdivia^{1,2}, Anaëlle Maury¹, and Patrick Hennebelle¹

¹ Laboratoire AIM, Paris-Saclay, CEA/IRFU/SAP - CNRS - Université Paris Diderot, 91191 Gif-sur-Yvette Cedex, France

² Department of Physics, Nagoya University, Furo-cho, Chikusa-ku, Nagoya, Aichi 464-8602, Japan
e-mail: valdivia.valeska@g.mbox.nagoya-u.ac.jp

Received Month dd, yyyy; accepted Month dd, yyyy

ABSTRACT

Context. High resolution (sub-) millimeter polarization observations have opened a new era in the understanding of how magnetic fields are organized in star forming regions, unveiling an intricate interplay between the magnetic fields and the gas in protostellar cores. However, to assess the role of the magnetic field in the process of solar-type star formation, it is key to be able to understand to what extent these polarized dust emission are good tracers of the magnetic field in the youngest protostellar objects.

Aims. In this paper, we present a thorough investigation of the fidelity and limitations of using dust polarized emission to map the magnetic field topologies in low-mass protostars.

Methods. To assess the importance of these effects, we have performed the analysis of magnetic field properties in 27 realizations of MHD models following the evolution of physical properties in star-forming cores. Assuming a uniform population of dust grains which sizes follow the standard MRN, we analyze the synthetic polarized dust emission maps produced if these grains align with the local B -field thanks to Radiative Torques (B-RATs).

Results. We find that (sub-)millimeter polarized dust emission is a robust tracer of the magnetic field topologies in inner protostellar envelopes and is successful at capturing the details of the magnetic field spatial distribution down to radii ~ 100 au. Measurements of the line-of-sight averaged magnetic field line orientation using the polarized dust emission are precise to $< 15^\circ$ (typical of the error on polarization angles obtained with observations from large mm polarimetric facilities such as ALMA) in about 75 – 95% of the independent lines of sight peering through protostellar envelopes. Large discrepancies between the integrated B -field mean orientation and the orientation reconstructed from the polarized dust emission are mostly observed in (i) lines of sight where the magnetic field is highly disorganized and (ii) lines of sight probing large column densities. Our analysis shows that high opacity of the thermal dust emission and low polarization fractions could be used to avoid utilizing the small fraction of measurements affected by large errors.

Key words. polarization – magnetic fields – protostars

1. Introduction

The fate of the evolution of protostellar cores is the result of the interplay between the gravity, turbulence, magnetic fields, chemical composition, through coupled processes that control the dynamics of the gas as well as its thermo-dynamical state. So to better understand the star formation process and to untangle the different contributions we rely on one hand on observations and on the other hand, on theoretical models. The quality of the modeling, as well as the quality of the interpretation of actual observations depend on how well we can connect these two approaches, making the study of how observed data actually traces the physico-dynamical state of the gas a key topic in modern astrophysics.

Particularly, magnetic fields (B -fields) are a fundamental component of the star formation process at all scales and evolutionary stages. They are key agents to regulate the star formation at scales of molecular clouds, by providing a support against the gravitational collapse (Mouschovias & Ciolek 1999; Li et al. 2014) and are thought to channel the mass accretion to form interstellar filaments (the preferred sites of star formation). At core scales ($\lesssim 3000$ au), if B -fields are efficiently coupled with the protostellar envelope made of dust and gas, they may also play a key role regulating the final outcome of star formation process, by transporting a significant fraction of the core angular momen-

tum outward, hence allowing the formation of stars, setting the pristine disk size and shaping the properties of the upcoming star and planets.

While observing the B -fields in star-forming environments cannot be done directly, various techniques have been developed to probe the magnetic properties in astrophysical structures. Among them, the most widely used for the dense molecular conditions consists in interpreting the polarized emission of ISM dust grains. Indeed, several theoretical works have suggested that non-spherical dust grains spinning around their axis of maximal inertia (the shortest axis of the dust grain), tend to align with the magnetic fields through dissipative processes producing a polarized dust emission that is perpendicular to the magnetic field lines (Davis & Greenstein 1951b; Purcell 1979; Roberge 2004). The mechanisms able to align the dust grains in such manner include the Radiative Alignment Torques (B-RATs, Lazarian & Hoang 2007a; Andersson et al. 2015), a new variant of RATs including superparamagnetic dust grains (MRAT, Hoang & Lazarian 2016), the supersonic mechanical grain alignment (or Gold effect, Gold 1952), the Mechanical Alignment Torques (MATs, Davis & Greenstein 1951a; Lazarian & Hoang 2007b), but other mechanisms (not discussed in this paper) operating at specific conditions may produce a polarized signal that do not necessarily trace the magnetic field. For instance, the dust self-scattering

(Kataoka et al. 2015), due to scattered light of anisotropic continuum emission by large dust grains (with sizes comparable to the observed wavelengths) can explain the polarization levels observed in the innermost regions of protostellar disks independently of the magnetic field, as well as another variant of the RAT theory (k-RATs, Lazarian & Hoang 2007b; Tazaki et al. 2017), where dust grains in regions near a strong radiation source precess around the radiation anisotropy vector instead of precessing around the magnetic field lines.

Current observations with single dish instruments (such as Planck, BLASTPOL and the JCMT POL2), as well as interferometric facilities (such as ALMA, CARMA and SMA) are providing a wealth of polarimetric data that, if properly interpreted, can deepen our insight on the different processes occurring in different environments. For instance, recent interferometric observations with the SMA have allowed Galametz et al. (2020) to highlight the potentially crucial role of the relative orientation between the magnetic field orientation, inferred from the polarized dust emission, and the rotation axis, inferred from the direction of the outflows and jets, on the fragmentation and multiplicity properties of protostars. Even though the ability of the polarized signal arising from aligned dust grains to trace the orientation of the magnetic fields is well established for the interstellar gas, it is still necessary to assess its robustness as a tracer of the magnetic field topology in the case of objects displaying a higher degree of complexity such as young protostars, since important conclusions are drawn from polarimetric observations, such as in the previously cited work.

Specifically, polarimetric observations aiming at probing the magnetic fields of protostellar cores face several challenges. As the collapse proceeds, the magnetic field lines are dragged, bent and distorted, difficulting the definition of a true mean orientation. The increasing gas density subsequently rises the opacity to levels where even at mm wavelengths it is hard to trace the full information along the line of sight. On the other hand, the properties of polarized dust emission heavily rely on the ability of dust grains to align with the magnetic fields: local irradiation and sut properties may affect how accurately the polarized dust emission represents the mean integrated orientation of the magnetic field lines. Understanding how well and under which conditions the magnetic field morphologies are constrained by polarimetric observations, can help us to understand the relative importance of the physical processes shaping the star formation process.

2. Methods

2.1. Non-ideal MHD models of protostellar cores

Protostellar cores are expected to display a wide variety of physical conditions, especially in terms of masses, level of turbulence, magnetization degree, and level of rotation and relative orientation between the magnetic field and the rotation axis. While an exploration of the complete parameter space is out of the scope of this study, we thrive to use realistic models of Class 0 protostars to investigate whether polarized dust emission is a reliable tracer of the magnetic field topology inside protostellar envelopes. We thus use a subset of the physically motivated numerical simulations by Hennebelle et al. (2020), which were initially run to understand how the interplay between the turbulence, magnetization degree, initial rotation and the initial angle between rotation axis and the magnetic field orientation define the outcome of the evolution of protostellar cores. They are believed to grasp the complexity of the physical process at work at

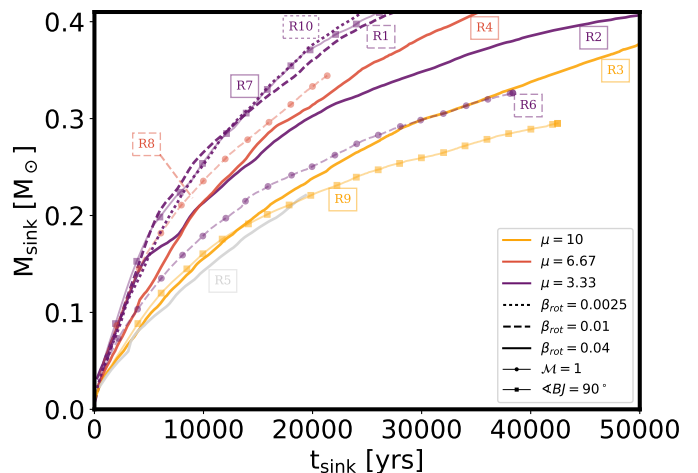


Fig. 1. Sink mass evolution as a function of the time since the formation of the sink t_{age} . The color identifies the normalized mass-to-flux ratio, the line-style identifies the rotational to gravitational energy ratio, and the symbols indicate the presence of turbulence (circles) or an extreme inclination of the rotation with respect to the magnetic field (squares). We keep the same identifiers in the following figures.

envelope scales, and hence can be trusted as realistic 3D models of the density, temperature, gas kinematics and magnetic field structures in prototypical solar-type Class 0 protostars.

The numerical simulations were performed using the RAMSES code (Teyssier 2002; Fromang et al. 2006), able to solve the MHD equations, including the ambipolar diffusion, to treat the gas dynamics. The thermal evolution of the gas is computed using an Equation of State (EoS) that mimics the opacity effects on the radiative transfer in dense gas (see Eq. 1 of Hennebelle et al. 2020). A sink particle approach is used to follow the formation and evolution of the protostar (Bate et al. 1995; Bleuler & Teyssier 2014). The code benefits from the adaptive mesh refinement (AMR) technique to adapt the resolution. In these simulations the refinement criterion is the local Jeans mass, which is required to be resolved by at least 20 cells. The structure of the data is a fully threaded ocTree. The set-up of the simulations is the same of Hennebelle et al. (2016) and Masson et al. (2016), with the difference that it includes sink particles and cover a wider range of initial conditions.

All the model cores have an initial mass of $1 M_{\odot}$, and the magnetic field is initially uniform and aligned with the z direction. The ratio of thermal to gravitational energy is $\alpha = 0.4$ for all the simulations. The selected models cover three levels of rotation (set by the ratio of rotational to gravitational energy $\beta_{\text{rot}} = E_{\text{rot}}/E_{\text{grav}} = 0.0025, 0.01, 0.04$), three levels of magnetization (given by the mass-to-flux ratio normalized to the critical mass-to-flux ratio $\mu = (M/\Phi)/(M/\Phi)_{\text{crit}} = 3.33, 6.67, 10.0$). Most of the models have a Mach number $\mathcal{M} = 0$ and an inclination between the initial rotation axis and the initial magnetic field orientation $\theta = 30^\circ$, but special cases including turbulence ($\mathcal{M} = 1$) and cases using an extreme tilt of $\theta = 90^\circ$ are also included. The runs identifiers (ID) as well as their parameters are summarized in the first part of Table 1.

Table 1. Parameters of the protostellar models

ID	μ	β_{rot}	θ	\mathcal{M}	t_{form} [yr]	$t_{0.1M_{\odot}}$ [yr]	$t_{0.2M_{\odot}}$ [yr]	$t_{0.3M_{\odot}}$ [yr]
R1	3.33	0.01	30°	0	55428	2493	5991	13484
R2	3.33	0.04	30°	0	60328	2472	8760	19509
R3	10.0	0.04	30°	0	50987	5179	14816	30282
R4	6.67	0.04	30°	0	51206	3693	8927	17943
R6	3.33	0.01	30°	1	66942	3618	12321	30486
R7	3.33	0.04	90°	0	56006	2461	6001	13532
R8	6.67	0.01	30°	1	57132	2460	7331	16413
R9	10.0	0.04	90°	0	49636	5112	15843	42005
R10	3.33	0.0025	30°	0	52577	2828	7015	12982

Notes. Selected numerical models from Hennebelle et al. (2020). μ is the mass-to-flux ratio normalized by the critical value, β_{rot} is the ratio between rotational energy and gravitational energy, θ is the inclination angle of the initial rotation axis with respect to the magnetic field axis, and \mathcal{M} is the initial Mach number. t_{form} is the time at which the sink forms in the simulation, while $t_{0.1M_{\odot}}$, $t_{0.2M_{\odot}}$ and $t_{0.3M_{\odot}}$ are the age of the sink at which it reaches 0.1, 0.2, and 0.3 M_{\odot} , respectively.

2.2. Protostar mass evolution and output selection

As the gravitational collapse proceeds, the density increases towards the center of the simulation box. When the local density reaches a threshold of $n_{\text{thres}} = 3 \times 10^{13} \text{ cm}^{-3}$, a sink particle is created at the highest resolution level, at the peak of the local clump formed by the neighboring cells whose density is higher than $n_{\text{thres}}/10$. The time at which the sink forms in the simulation, shown in the sixth column of Table 1, indicates how fast these conditions are reached. The sink particle mimics the formation and evolution of the protostellar embryo, allowing us to follow its mass evolution and dynamics. The sink formation happens faster for the less magnetized models (R9 and R3), while the slowest formation corresponds to the R6, which in addition to being more magnetized ($\mu = 3.33$) and having a moderate rotation ($\beta_{\text{rot}} = 0.01$), is turbulent. The importance of the additional support against collapse provided by the rotation itself is reflected on the delayed formation time of the sink in models R1, R2 and R10 that, in spite of having the same initial parameters except for the rotation, increases with β_{rot} .

The sink particle can further increase its mass by accreting gas from neighboring cells within a radius of 4 times the size of the most refined grid nearby the sink position. At each timestep and in each cell of its neighborhood, the sink accretes 10% of the gas whose density is above $n_{\text{thres}}/3$. The sink mass evolution shown in Fig. 1 seems to indicate that the most important parameter in terms of the accretion is the mass-to-flux ratio. But contrary to the trend seen for the sink formation time, the initial accretion proceeds faster in the more magnetized cases as a consequence of the formation of more massive disks when the magnetic field is weaker and rotation stronger. All in all, an increasing B -field delays the formation of the protostellar embryo at the center of the collapsing core, but allow the early mass accretion on the protostar to proceed faster. Although other processes may be playing a role as well, note that the two least magnetized simulations (R9 and R3) have the earliest sink formation, and show the lowest mass accretion rates. The strength and geometry of the magnetic field also can play a more episodic role during the protostellar formation process: for example simulation R2 exhibits a reduced mass accretion rate when its sink particle has reached roughly 0.15 M_{\odot} . This can be explained by the development of a magnetic cavity (the loop-like structure seen in the $x - y$ map of Fig. 2), consequence of the interchange instability (Krasnopolsky et al. 2012), often seen in simulated disks (Matsumoto et al. 2017; Machida et al. 2014; Joos et al. 2012; Seifried et al. 2011).

In order to analyze and compare simulations with such different evolution, we use the fraction of the initial mass core accreted onto the stellar embryo (traced by the sink mass) as an indicator of the evolutionary stage of the protostar-envelope system. For each simulation we have selected three snapshots that corresponds to the moment when 10%, 20% and 30% of the initial core mass has been transferred to the embryo, or equivalently, the sink mass, m_{sink} , has reached 0.1, 0.2, and 0.3 M_{\odot} , respectively, thus sampling the Class 0 stage ($M_{\text{env}} > M_{\text{star}}$). The time at which the sink forms in each simulation (t_{form}), as well as the age at which the sink reaches the selected masses relative to its formation time are shown in the right hand side of Table 1. The general evolution of the sink mass for all the simulations is shown in Fig. 1. We decided not to use the very weakly magnetized run R5 since it fragments early in the evolution and none of the fragments reaches 0.3 M_{\odot} .

2.3. Magnetic field mean orientation using bidirectional statistics

Since dust grains with opposite spinning directions produce an identical polarized pattern, the polarized dust emission is insensitive to the direction of the magnetic field, and, as a consequence, the magnetic field orientation can be considered as a bidirectional quantity. When the data is diametrically bimodal the mean angle obtained by computing the mean projected sinus and cosinus is orthogonal to the actual mean orientation due to cancelling effects. For example, toroidal magnetic field lines will produce a poloidal field geometry when they are computed edge-on because lines in the foreground and on the background have opposite directions that will cancel out.

Even though the usual integrated magnetic field in simulations of interstellar gas seems to satisfactorily trace the mean orientation, it is not well adapted to describe the mean orientation in regions where the magnetic field lines are particularly tangled, as in the case of protostellar cores, due to the aforementioned cancelling effects. Since this effect extends into the envelope of protostellar cores it is necessary to find a suitable description of the magnetic field mean orientation compatible with the polarized dust emission.

Here, and in the following, we compute the orientation angle, and any other angle, as the position angle with respect to the northern (vertical) direction, in the sense that increases anticlockwise, as recommended by the IAU, in the range -90° to $+90^\circ$.

To compute the mean orientation of the magnetic field, we borrow a statistical technique widely used in geography to treat bimodal orientation data (Jones & James 1969; Mardia 1975). In order to calculate the mean orientation of the magnetic field lines along the line of sight regardless of the direction of the B -vectors we proceed to double the individual angles and to compute the density weighted mean sinus and cosinus of $2\phi_B$, where ϕ_B is the local magnetic field angle projected onto the plane of the sky, as follows:

$$\langle \sin(2\phi_B) \rangle = \frac{\int_{los} \rho \sin(2\phi_B) dl}{\int_{los} \rho dl} \quad (1)$$

$$\langle \cos(2\phi_B) \rangle = \frac{\int_{los} \rho \cos(2\phi_B) dl}{\int_{los} \rho dl}, \quad (2)$$

where ρ is the local gas number density, and the averages are computed along the line of sight los . The mean orientation of the magnetic field $\langle \phi_B \rangle$ is then calculated as:

$$\langle \phi_B \rangle = 0.5 \arctan(\langle \sin(2\phi_B) \rangle, \langle \cos(2\phi_B) \rangle). \quad (3)$$

The angle doubling procedure is consistent with analytical formulae to compute the Stokes parameters Q and U , such as described in Landi Degl'Innocenti & Landolfi (2004) or Martínez González et al. (2011).

To estimate the intrinsic level of organization of the magnetic field lines along the line-of-sight we define the circular variance V_ϕ as follows:

$$V_\phi = 1 - \sqrt{\langle \sin(2\phi_B) \rangle^2 + \langle \cos(2\phi_B) \rangle^2}. \quad (4)$$

Clustered values of ϕ_B will produce circular variance values close to 0, while an increasing dispersion of angles (or in other words an increasing level of disorganization) will produce values closer to 1. Figure C.1 shows the relation between the circular variance V_ϕ and the typical standard deviation σ_ϕ in degrees.

2.4. Polarized dust emission with the dust radiative transfer code POLARIS

2.4.1. RAMSES datacubes

We use the subset of the simulations presented in Hennebelle et al. (2020) summarized in Table 1. Each RAMSES output provides a datacube containing the gas density, the gas pressure (or equivalently the gas temperature), the three components of the velocity field, as well as the three components of the magnetic field. These gas properties are extracted and put in a suitable format to be post-processed with POLARIS. To facilitate the propagation of photons and avoid missed photon packages from the central source due to long computational times, we artificially emptied a small central sphere of radius 4 au around the sink particle as in Valdivia et al. (2019). This procedure (only performed for the radiative transfer in post processing) is a pragmatic choice to allow a faster radiative transfer despite of the very optically thick layers surrounding the sink, minimizing computational artifacts and thus improving the quality of the radiative transfer at the scales studied in this paper (50 – 4000 au). As most of the reprocessing of the protostellar photons into infrared photons happens at radii 4 – 10 au, this procedure does not affect noticeably the temperature and irradiation spectrum at the scales we are investigating in this study.

To describe the evolution of the simulated collapse we provide integrated maps of the total column density (N), total mean

Table 2. Summary of the parameters used in POLARIS for all the models described in Table 1.

Quantity	Symbol	Value
<i>Radiation sources</i>		
Central source Luminosity	L_{star}	1 L_\odot
Central source radius	R_{star}	1 R_\odot
External radiation field	G_0	1 (Mathis et al. 1983)
<i>Synthetic observation parameters</i>		
Distance to observer	D	250 pc
Wavelengths	λ	0.8, 1.3, 3.0 mm
Map size	L_{map}	8000 au
Resolution	dx	5 au
<i>Dust parameters</i>		
Gas to dust ratio	ρ_g/ρ_d	100
Minimum grain size	a_{min}	5 nm
Maximum grain size	a_{max}	20 μm
Aspect ratio	ϵ	0.5 (oblate)
Power-law index ^a	α	-3.5
Astronomical silicates	f_{sil}	62.5 %
Graphite	f_{graph}	37.5 %
Suprathemal dust ^b	$f_{\text{high-J}}$	0.25

Notes. ^(a) Power-law index of the size distribution $dn(a) \propto a^\alpha$, ^(b) Fraction of dust grains spinning suprathermally.

magnetic pressure (P_{mag}) and mean magnetic field orientation (ϕ_B), as well as the associated circular variance (V_ϕ) at key time-steps in Sect. 3. We point out that the advantage of providing the mean magnetic pressure (P_{mag}) rather than the mean magnetic field is that it reflects the strength of the magnetic field without cancelling out the contributions of vectors with opposite directions. The mean magnetic pressure is computed as the density weighted average of the local magnetic pressure, P_{mag} , which is given by:

$$P_{\text{mag}} = \frac{B^2}{8\pi} = \left(\frac{B}{5 \mu\text{G}} \right)^2 \times 10^{-12} \text{ erg cm}^{-3}, \quad (5)$$

where $B = \sqrt{B_x^2 + B_y^2 + B_z^2}$ is the local magnetic field strength in micro Gauss.

2.4.2. Radiation sources and dust properties

For all the simulations, and regardless of the protostar mass, we model the central radiation source as a blackbody of 1 L_\odot of radius of 1 R_\odot located at the sink position. For a more detailed study investigating the dependency of dust polarized emission with varying accretion luminosity, and associated radiation field penetrating the envelopes of Class 0 protostars, see e.g. Le Gouellec et al. 2020 and Le Gouellec et al. in prep. We include an external isotropic radiation field of strength $G_0 = 1$ following the Mathis et al. (1983) description.

The dust properties are assumed uniform throughout the simulation box and are the same than in Valdivia et al. (2019), namely a gas-to-dust ratio of 100, with a composition of 62.5 per cent of astronomical silicates and a 37.5 per cent of graphite grains that matches the Galactic extinction curve (Mathis et al. 1977). The dust grains are supposed oblate with an aspect ratio of 0.5 (Hildebrand & Dragoon 1995) and following a power-law size distribution (Li & Draine 2001) of

$$dn(a) \propto a^{-3.5} da, \quad (6)$$

where a is the effective dust radius of a spherical grain of equivalent volume, and $n(a)$ is the number of dust grains of effective radius a . The lower and upper cutoff of the size distribution are set as $a_{\min} = 5$ nm and $a_{\max} = 20$ μ m, respectively. The choice of a_{\max} stems from a compromise between our previous study (Valdivia et al. 2019), suggesting that the polarization fractions observed towards protostellar cores can only be approached when including a population of large grains, and the need to avoid the regime of very large grains where the DDSCAT (Draine & Flatau 2000) introduces artifacts on the absorption coefficients (see Reissl et al. 2016).

All the parameters are summarized in Table 2 and are the same used for all the selected snapshots.

2.4.3. Temperatures and dust alignment with POLARIS

We post-process each one of the snapshots described in Sect. 2.1 with the POLARIS code (Reissl et al. 2016). The photon propagation is based on a Monte Carlo scheme and, along with the local values of the density and the magnetic field, it is used to compute the dust temperature and the grain alignment efficiency on a cell by cell basis. Since the gas temperature computed by RAMSES using an EoS is the result of an approximation and not the result of an actual radiative transfer, we recompute the gas temperature as well.

In addition to the gas and dust heating, the radiation field induces a radiation torque on dust grains, spinning them up to suprathermal rotation velocities, at which they can align with the magnetic field (Barnett 1915; Dolginov & Mitrofanov 1976; Lazarian & Hoang 2007a; Hoang & Lazarian 2014).

The grain alignment efficiency is computed according to the B-RATs theory as implemented in POLARIS (Reissl et al. 2016). In principle, the fraction of dust grains spinning at suprathermal velocities ($f_{\text{high-}J}$, which is the stable population of aligned grains), depends on the dust grain properties such as the specific shape, composition, and magnetic properties. Since this quantity cannot be calculated exactly, it is set as $f_{\text{high-}J} = 0.25$. This rather conservative choice is able to produce a detectable amount of polarization. Recently Herranen et al. (2021) have found that the alignment efficiency might be higher than predicted, and that for aggregates $f_{\text{high-}J} \sim 0.35 - 1$ (Herranen et al. 2021), and the presence of iron inclusions can increase this quantity to unity (Hoang & Lazarian 2016). Additionally, we take into account the fact that due to internal thermal fluctuations non-spherical dust grains are not expected to be perfectly aligned, but precessing around their rotation axes, by enabling the imperfect internal alignment mechanism (II, Barnett 1915; Purcell 1979), as implemented in POLARIS. To include the effect of random gas collisions, we include the imperfect Davis-Greenstein alignment (IDG, or paramagnetic relaxation Davis & Greenstein 1951b; Jones & Spitzer 1967; Purcell 1979; Spitzer & McGlynn 1979), which despite of being rather inefficient (Reissl et al. 2017), can contribute to align a part of the small grains. Silicate grains and graphite grains have very different paramagnetic properties, which differ by roughly six orders of magnitude (Draine 1996; Hoang & Lazarian 2014). This results in a very randomized distribution of graphite grain orientations, preventing them to contribute to the polarized emission. Finally, we do not include the effects of the self-scattering (Kataoka et al. 2015), since it operates in the innermost regions of the disk (typically within a radius of ~ 10 au), which are excluded from our analysis, nor the alignment with the radiation field (Lazarian & Hoang 2007b; Tazaki et al. 2017).

2.4.4. Synthetic observations of the Stokes maps with POLARIS

For each one of the selected snapshots we set our model at a distance of 250 pc and we observe a squared region of 8000 au side centered at the position of the protostellar embryo (materialized by the sink particle) at a resolution of 5 au per pixel. Each snapshot is observed synthetically along each one of the main axes x , y , and z (y - z , x - z , and x - y maps respectively) at three wavelengths: 0.8, 1.3 and 3.0 mm.

For each synthetic observation, POLARIS provides perfectly observed maps of the four components of the Stokes vector $S = (I, Q, U, V)^T$, where I is the total dust emission, Q and U are the linearly polarized dust emission components, and V is the circularly polarized emission.

Finally, we compute the total linearly polarized intensity maps (PI) and the polarization fraction p_{frac} from the Stokes maps as follows:

$$PI = \sqrt{Q^2 + U^2} \quad (7)$$

$$p_{\text{frac}} = PI/I. \quad (8)$$

At far-IR to millimeter wavelengths, the magnetic field orientation inferred from the polarized emission (ϕ_{pol}) is obtained by rotating by 90° the polarization vector $\psi = \frac{1}{2} \arctan(U, Q)$.

3. From 3D models to 2D maps: evolution of the integrated properties in the models

The general evolution of the numerical simulations and the dependence on the initial conditions is detailed in Hennebelle et al. (2020). In this paper we focus on the description of the properties relevant to the polarized dust emission, particularly the protostar evolution (represented by the sink particle), the column densities, the integrated mean orientation of the magnetic field lines, as well as its intrinsic degree of disorganization (quantified by the variance of the angle orientation along the line of sight).

3.1. Integrated 2D maps and radial profiles

In this section we present integrated maps along the x , y and z axes for the selected simulations and snapshots described in Table 1. We chose to present these maps at the same resolution and scale than that of the synthetically observed ones to allow a direct comparison between both. In Fig. 2 we present the total column density maps, that correspond to the total amount of hydrogen atoms integrated along the line of sight. Fig. 3 shows the density-weighted mean magnetic pressure (P_{mag} , as described in Sect. 2.4.1) with overlaid mean orientation (ϕ_B , computed following Eq. 3), aiming at providing a description of the magnetic field strength and mean orientation. Figure 4 shows the circular variance (V_ϕ , as defined in Eq. 4), that quantifies the level of disorganization of the magnetic field lines along the line-of-sight. Finally, we summarize these results by computing the average radial profiles of the three axes of N and V_ϕ in Figs. 5 and 6 respectively.

The column densities shown in Fig. 2 display a wide variety of gas distribution features including outflows, spiral structures, loops and more complex density distributions depending on the initial physical conditions. More precisely, the simulations including turbulence display very asymmetrical features,

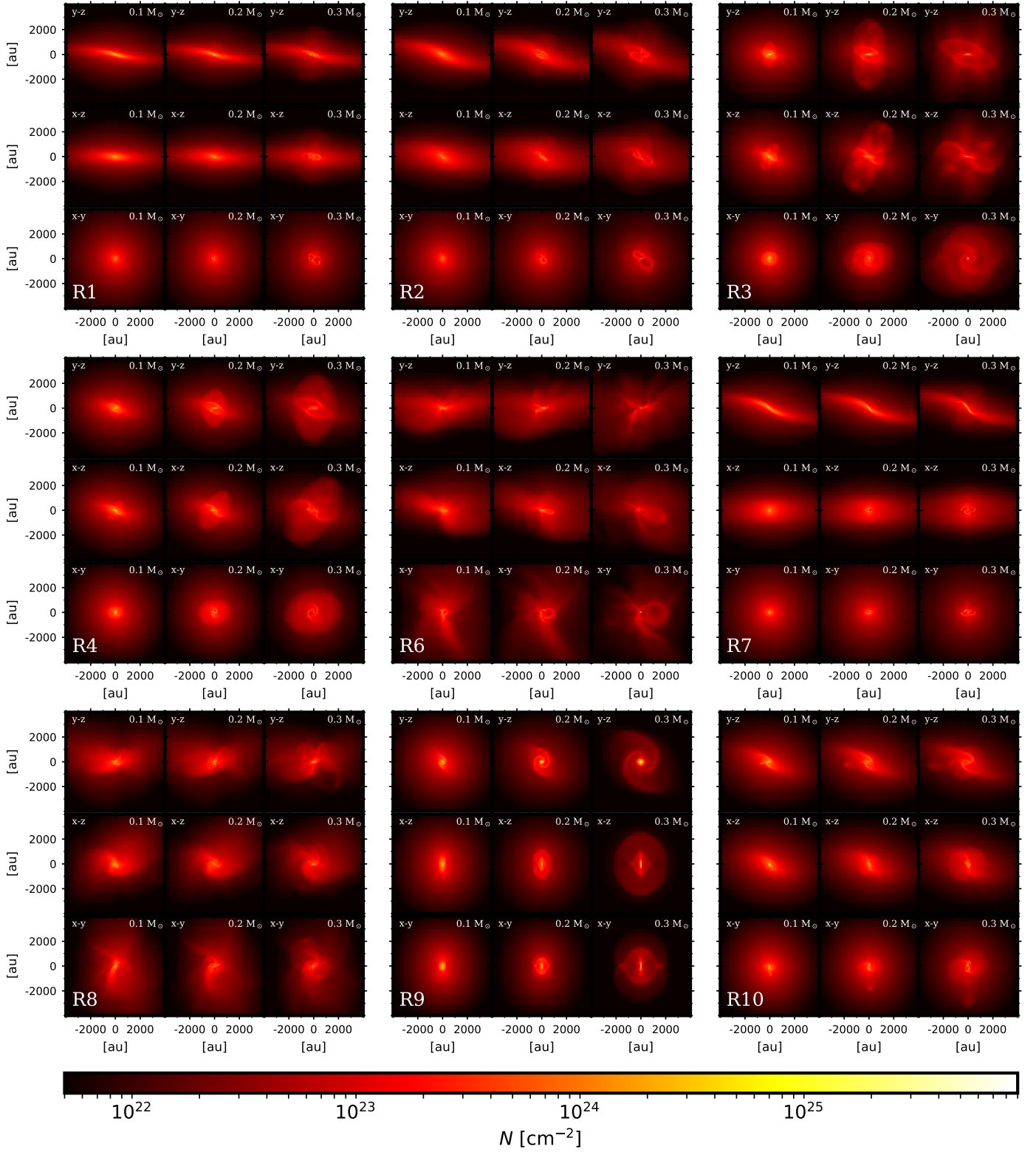


Fig. 2. Column density maps of all the selected outputs described in Table 1. Each block corresponds to a given simulation (the identifier is indicated on the lower left corner of the block). Each block displays column density maps integrated along the x , y and z axes (from top to bottom: y - z , x - z , and x - y maps, respectively), and for a snapshot at $m_{\text{sink}} = 0.1, 0.2$, and $0.3 M_{\odot}$ (from left to right). The projection and evolutionary step are shown at the top of each individual plot.

while the rest of the simulations show more uniform ones. Figure 3 shows how after the initial gravitational collapse the magnetic field lines are dragged forming the characteristic hourglass shape, but the further evolution of the gas distribution and the

final morphology of the magnetic field are controlled by the interplay of the specific physical conditions. As in the case of the evolution of the sink particle, the most important parameter is the mass-to-flux ratio (μ). Figure 3, and more particularly simu-

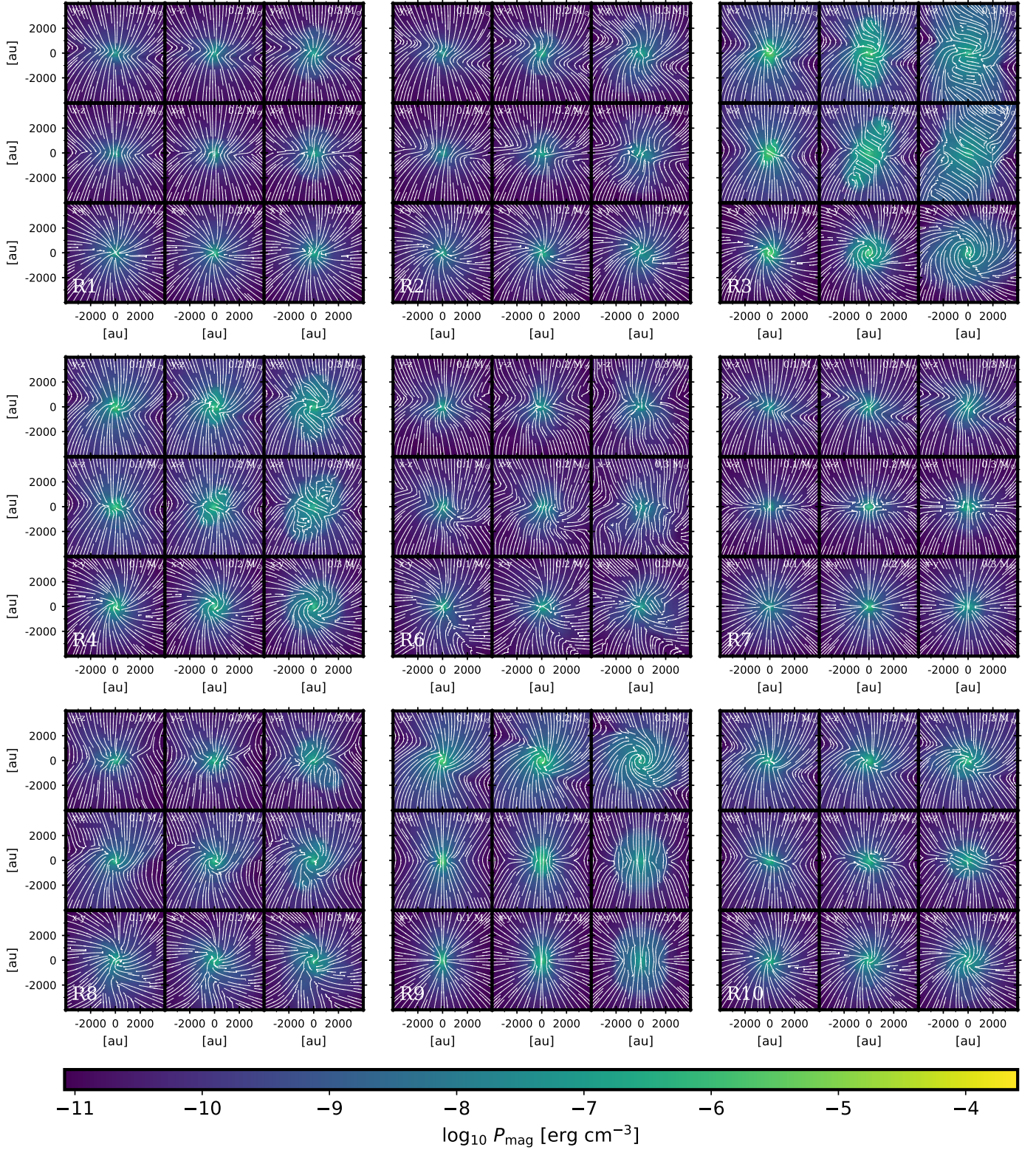


Fig. 3. Mean magnetic pressure P_{mag} maps and the orientation of the magnetic field lines along each projection for all the simulations. Each block corresponds to a given simulation and the plots are organized using the same structure than for Fig. 2.

lations R2, R3 and R4, shows that since the magnetic field lines are more prone to be bent and distorted in the less magnetized cases ($\mu = 10$), the magnetic field lines evolve into a helicoidal morphology in the outflow, which develops more easily. As the magnetization level increases, the outflow remains more confined and the helicoidal feature is less evident. The effect of the

magnetization level can also be seen in simulations R7 and R9. Both simulations have the same rotation parameters ($\beta = 0.04$ and $\theta = 90^\circ$), but the outcome of the evolution is very different. Simulation R9 ($\mu = 10$) displays a well developed spiral structure seen in the $y-z$ projection (nearly face-on projection) of the column density map shown in Fig. 2 as well as in the projected

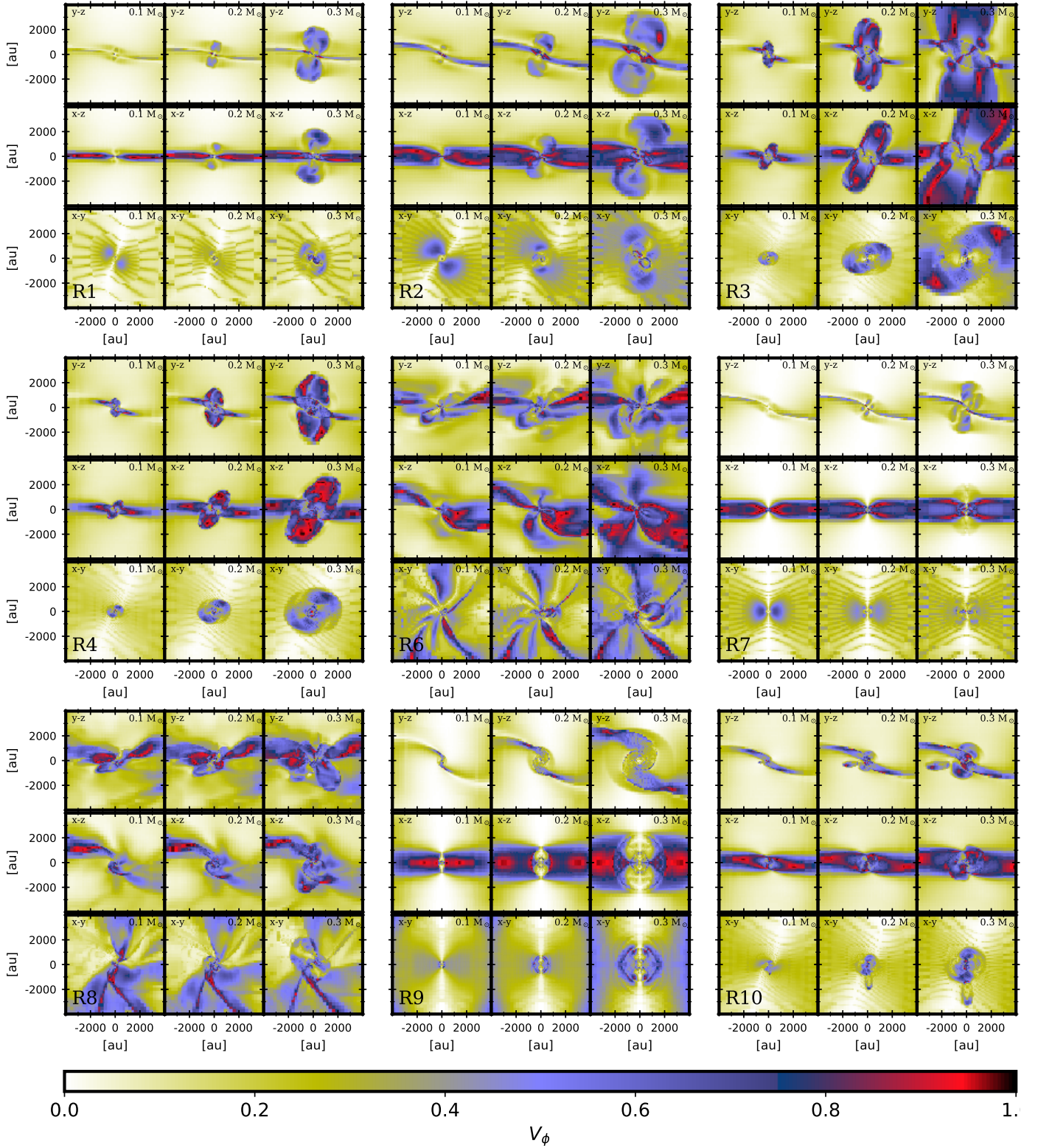


Fig. 4. Circular variance V_ϕ of the B -field lines in the RAMSES data cubes (See Sect. 2.3). The figure is organized using the same structure than for Figs. 2 and 3. The simulation identifier is given at the bottom left corner of the block, while the projection and evolutionary step are shown at the top of each individual plot.

magnetic field lines (streamplot) of Fig. 3. On the other hand, in simulation R7 the stronger magnetic tension inhibits the development of high-contrast density waves seen as spiral arms, and the associated warped B -field lines. Simulations R6 and R8 also share the same rotation ($\beta = 0.04$ and $\theta = 30^\circ$) and turbulent

($\mathcal{M} = 1$) parameters, but in this case it seems that the turbulence dominates the evolution of the gas dynamics as well as the evolution of the magnetic field lines. Nevertheless, the circular variance (Fig. 4) seems to be higher and more extended for R6.

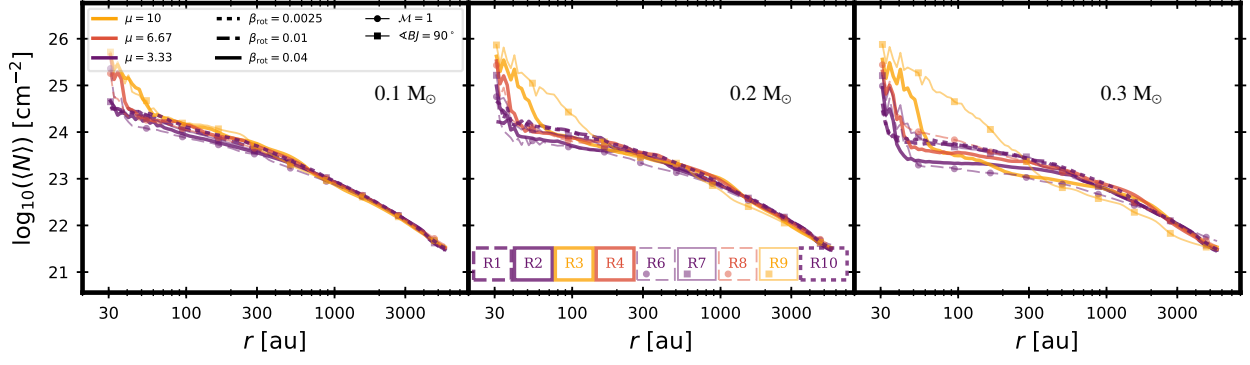


Fig. 5. Radial mean column density profiles. From left to right: profiles at $m_{\text{sink}} = 0.1, 0.2$, and $0.3 M_{\odot}$.

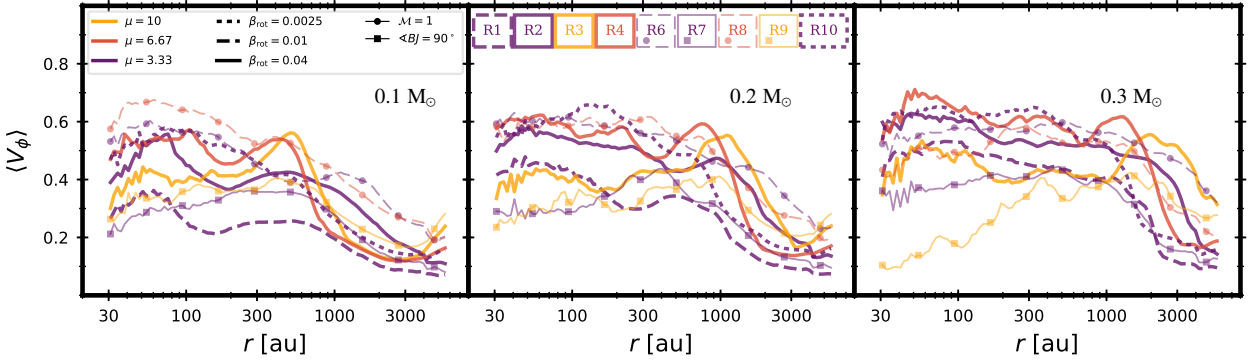


Fig. 6. Radial mean profiles of the circular variance V_{ϕ} . From left to right: profiles at $m_{\text{sink}} = 0.1, 0.2$, and $0.3 M_{\odot}$.

The circular variance maps (Fig. 4) describe the level of organization of the projected orientation of the magnetic field lines onto the plane of the sky, while traveling along the line-of-sight. Since all the magnetic field lines are initially set parallel to the z direction, all the V_{ϕ} maps are initially uniform and equal to 0. As the gas collapses inwards dragging the magnetic field lines, the projected orientations of the magnetic field are not parallel anymore and the V_{ϕ} starts to increase. At larger scales ($r > 4000$ au, not shown in the figure) the magnetic field orientation remains extremely well organized and the hourglass pattern is barely affected by the rotation or the outflow. At smaller scales, as those shown in the figure, the magnetic field remains relatively ordered along the lines-of-sight exhibiting yellow to light blue colors, that correspond to a typical angular dispersion of the orientation of the magnetic field of $\sigma_{\phi} = 20^{\circ} - 30^{\circ}$ (see Appendix C), while regions with purple to red have larger angular dispersions ($\sigma_{\phi} > 30^{\circ}$). These regions of larger V_{ϕ} are ubiquitously seen towards the midplanes of the nearly edge-on projections, as well as in regions where the early hourglass structure of the magnetic field is perturbed either by the development of the outflow (very prominent in simulations R2 and R3, for example) or by the turbulent gas motions (simulations R6 and R7).

Note that the projection that displays the most organized B -field is z ($x - y$ maps on the bottom row of each block,) which is the direction of the initial magnetic field lines (V_{ϕ} remains small even for the cases R7 and R9 where the rotation axis is tilted by 90° with respect to z direction).

To summarize the global behavior of the simulations and to compare the time evolution of both the collapse and the stress it produces on the magnetic field topology, we compare the mean radial profiles of the total column density and of the circular variance of the B -field orientation (Figs. 5 and 6, respectively). For each evolutionary step and simulation we stack the integrated maps of the three projections, and compute the mean value of the variable in radial logarithmic bins. From the evolution of the column density radial distribution (Fig. 5) we clearly distinguish the usual development of a high density inner region peaking around the protostar (column densities higher than $\sim 2 \times 10^{24} \text{ cm}^{-2}$ within a radius of $r \lesssim 60$ au). We also notice a flattening of the density profile at intermediate radii with time, due to the development of a flattened envelope sometimes also referred to as the "pseudo-disk" (Galli & Shu 1993; Li & Shu 1996; Hennebelle & Ciardi 2009), while the outer layers of the protostellar envelopes ($r > 1000$ au) remain mostly unaffected. All the simulations, except for the simulation with a lower degree of magnetization, present a comparable global evolution. Simulation R9 and to a lower extent simulation R3 (low magnetization cases and $\theta = 90^{\circ}$ and $\theta = 30^{\circ}$, respectively), display a wider overdensity region due to the development of the spiral structures and a thicker equatorial region with respect to the rotation axis.

The behavior of the mean circular variance radial profiles of Fig. 6 seems quite different from that of the mean column density radial profile. The V_{ϕ} profiles have slightly lower values in the inner region, remaining more uniform with typical values of $V_{\phi} \sim 0.2 - 0.6$ at intermediate radii, while in the outer region

they decrease to unperturbed values. The regions displaying the largest variance are located at intermediate distances, following the development of the outflow. In these regions the development of a helicoidal magnetic field, along with the projection effects, induces a higher circular variance in the cavity walls of the outflow, as remarkably shown in the case of R3. However, even at advanced Class 0 evolution ($0.3 M_{\odot}$ in the central embryo) the stress applied by the gravitational collapse and outflowing motions to the B -field only result in rather low V_{ϕ} with values < 0.6 (equivalent to typical dispersion of the B -field angle along the line of sight $\lesssim 30^{\circ}$). A particular case is the simulation R9, that displays a decreasing V_{ϕ} with time in the inner ~ 500 au with time due to the development of a more organized spiral pattern guided by the rotation due to a lower magnetic tension, and that remains unperturbed due to the lack of outflow. There is not a clear dependence between the mean V_{ϕ} and the degree of magnetization, but the presence of turbulence seems to produce a more uniform and more stable level of disorganization of the magnetic field lines.

To better understand how the circular variance is related to the column density we compute the mean value of V_{ϕ} in logarithmic bins of total column density. Figure 7 shows these results for the stacked data. We notice that initially only the intermediate column densities present high levels of disorganization of the magnetic field lines. These regions are related to the equatorial region, where the column densities increase due to the collapse and the further accretion is guided along the magnetic field lines, at the same time that the lines are distorted by the gas rotation. At later times, as the gas becomes denser, regions with high V_{ϕ} develop at higher column densities for the simulations with higher degree of magnetization (purple lines indicating $\mu = 3.33$), for all the cases (with turbulence, or rotating orthogonal to the magnetic field). It is interesting to notice that simulations R3 and R9 (yellow lines), despite of having the same level of magnetization and rotation, differing only on the initial rotation angle, display a very different behavior at intermediate column densities, particularly at around $N \sim 10^{24} \text{ cm}^{-2}$, where the simulation R3 have values of $V_{\phi} > 0.6$, while simulation R9 barely surpasses 0.2.

4. Synthetic maps of the polarized dust emission

We produced perfectly integrated synthetic observations of the polarized dust emission for the central 8000 au, observed at a distance of 250 pc, and at a resolution of 5 au per pixel (see Table 2). In Fig. 8 we present synthetic maps observed at 1.3 mm of the polarization fraction (background color maps), with overlaid polarized intensity contours (normalized to the peak value) and the magnetic field vectors (inferred from the polarized emission as described in Sect. 2.4). To summarize and simplify the comparison between all the simulations we compute the radial profiles stacking the data for the integrated quantities along the three projections. We provide the radial profiles of the Stokes I , the intensity of the total linearly polarized dust thermal emission PI and the polarization fraction p_{frac} in Fig. 9. We present similar maps, but for $\lambda = 0.8$ and 3.0 mm (Figs. A.1 and A.2) as well as similar radial profiles (Figs. A.3 and A.4) in the Appendix. The total dust emission maps (Stokes I maps, not shown here) peak towards the central region neighboring the protostar, closely following the column density as expected. This is also seen by comparing the radial profiles of the Stokes I maps (top rows of Fig. 9 and A.3 and A.4) to the total column density maps (Fig. 5), that show a good agreement between these two quantities, but showing slight departures at high column densities due to the large associated opacities.

The total linearly polarized intensity (contour lines of Figs. 8, A.1 and A.2 and middle row panels of Figs. 9, A.3 and A.4) show higher values towards the central region (due to higher densities and temperatures), but the associated polarization fractions are the lowest in these regions (see the bottom panels of Figs. 9, A.3 and A.4). The highest polarization fractions are found in the external regions, typically reaching 5 to 10%, and gradually decrease in a non monotonically manner towards the central regions. More precisely, Fig. 8 show that p_{frac} drops more strongly in the midplane and the outflow regions, particularly near the cavity walls. Even though the outflow regions show lower polarization levels, the simulation R3 shows a rather high p_{frac} in the central part of the outflow region. This is likely due to the fact that the outflow cavity is well developed, allowing the transversal component of the helicoidal magnetic field to dominate the polarization pattern. A qualitative comparison of Fig. 6 and Fig. 8 suggest that the polarization fraction drops in the lines of sight where the B -field happens to have a large variance V_{ϕ}). In the following section, we quantify and discuss this behavior, and its consequences on our ability to trace the B -field in low-mass protostellar envelopes with dust polarization observations.

5. Do polarized dust emission maps capture the underlying topology of protostellar magnetic fields?

5.1. Fidelity of the inferred magnetic field orientation

This work aims at assessing whether (sub-)millimeter polarized dust emission maps of protostellar envelopes, routinely used to discuss the magnetic field at work during the collapse of protostellar cores into a star-disk system, are indeed robust tracers of the magnetic field lines threading those cores. To do so, we compare the two quantities introduced in Sect. 2: the magnetic field orientation reconstructed from the synthetic observation of polarized dust emission (ϕ_{pol} , Sect.2.4.4) with the mean orientation of the magnetic field in the model, integrated along the line of sight, and computed using the circular statistics (ϕ_B , Eq. 3). We compute the difference between model and observations as the following difference: $\Delta\phi = \phi_{\text{pol}} - \phi_B$, and the discrepancy as the absolute value of the difference, $|\Delta\phi|$.

5.1.1. Dust polarized emission: an overall good tracer of B -fields in protostellar environments

We build difference maps between the model magnetic field line orientations and the reconstructed magnetic field orientations from polarized dust emission observed at $\lambda = 0.8, 1.3$, and 3.0 mm (see Figs. A.5, A.6 and A.7, respectively). We notice that there is a general good agreement between the inferred (ϕ_{pol}) and the actual (ϕ_B) mean orientations, with localized regions displaying large differences. From these maps, we can quantify in a statistical way the ability of the polarized dust emission at recovering the true magnetic field topology. We define the recovery rate as the fraction of sight lines in a map for which the magnetic field orientation is retrieved within a given error, or in other words, have a discrepancy $|\Delta\phi|$ lower than a given threshold. This recovery rate is found to be similar at the three wavelengths for each map, slightly increasing with the wavelength. At $\lambda = 0.8$ mm, which is the frequency that displays the lowest recovery rates, the magnetic field is typically recovered within an error of less than 15° for more than 95% of the lines of sight over the full maps, with only some cases with no clear dependence on the magnetization level, rotation or

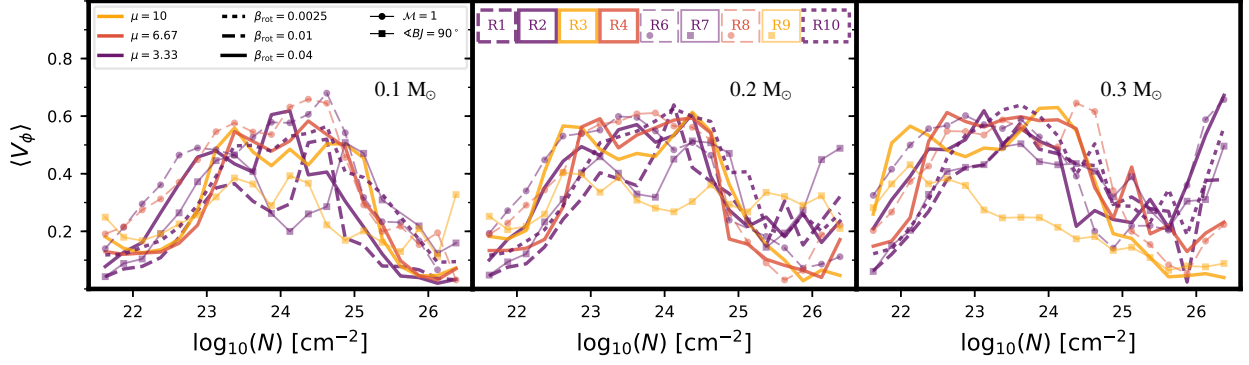


Fig. 7. Mean circular variance V_ϕ per logarithmic bin of column density. From left to right: results at $m_{\text{sink}} = 0.1, 0.2$, and $0.3 M_\odot$.

Table 3. Fidelity of B -field mapping from polarized dust emission at $\lambda = 0.8$ mm in protostellar envelopes at different scales.

m_{sink} [M_\odot]	B -field recovery rates and σ [%]							
	All scales		30 – 100 au		100 – 500 au		500 – 1500 au	
$\mu = 3.33$								
0.1	96.9	3.1	70.1	14.8	82.3	18.8	92.9	9.5
0.2	95.6	4.2	74.3	11.0	75.8	18.5	89.2	12.2
0.3	93.3	5.3	73.0	10.3	78.2	12.7	85.9	11.7
$\mu = 6.67, 10.$								
0.1	97.3	2.1	83.7	7.6	86.4	9.8	95.4	4.5
0.2	95.7	2.7	79.3	9.0	90.4	6.4	89.9	7.3
0.3	90.7	6.3	75.2	13.2	88.9	8.6	89.5	6.3

Notes. The recovery rate corresponds to the fraction of lines of sight where measurement of the B -field orientation from polarized dust emission recovers the integrated B -field orientation within an error of $< 15^\circ$ in the modeled Class 0 envelopes. The percentages shown in this table correspond to the averaged recovery rate, while the standard deviation of each measurement is given in a smaller font next to each mean value. The results are separated in two cases: moderate magnetic field ($\mu = 3.33$, simulations R1, R2, R6, R7, and R10) and weak magnetic field ($\mu = 6.67, 10.$, simulations R3, R4, R8, and R9). Percentages have been averaged over all the corresponding simulations and projections at a given evolutionary step (given by the protostar mass m_{sink}). The scales correspond to the whole map including all the scales (second column), and in concentric rings containing all the lines of sight with radial distances to the protostar in the interval indicated in the header of the table. All the individual recovery rates are given in Table A.1.

inclination, recovering less than 90%. These cases correspond to late evolutionary steps, and specially for the projections along the y -axis ($x - z$ maps), obtaining the worst recovery rate (79.7%) for simulation R3, $m_{\text{sink}} = 0.3 M_\odot$ and projected along the y -axis. For this map, most of the lines of sight for which the orientations were not recovered within an error of 15° are associated to higher circular variances (the recovery rate for the lines of sight with $V_\phi < 0.5$ is 99.7%). We summarize in Table 3 the mean recovery rates for the synthetic maps at $\lambda = 0.8$ mm at different evolutionary stages and at different scales, averaged for all the projections and simulations. The detailed results are given in Table A.1. These tables show that the magnetic field orientation reconstructed from polarized dust emission observations is remarkably good at large scales and that even at intermediate scales the recovery rate is typically higher than

Table 4. Fidelity of B -field mapping from polarized dust emission at $\lambda = 0.8$ mm in protostellar envelopes as a function of the polarized intensity.

m_{sink} [M_\odot]	B -field recovery rates and σ [%]					
	$PI_{\text{norm}} \geq 10^{-2}$		$PI_{\text{norm}} \geq 10^{-3}$		$PI_{\text{norm}} \geq 10^{-4}$	
$\mu = 3.33$						
0.1	84.4	17.7	93.3	8.8	98.4	2.0
0.2	83.7	14.2	92.7	8.4	97.7	2.5
0.3	86.6	8.9	92.7	6.3	96.5	3.3
$\mu = 6.67, 10.$						
0.1	92.9	4.3	95.6	3.7	99.0	1.0
0.2	93.6	4.4	94.0	3.8	98.0	1.6
0.3	92.2	6.0	93.8	4.7	95.4	3.6

Notes. The recovery rates are defined as in Table 3 for an error of $< 15^\circ$. The recovery rates shown in this table correspond to the mean values found for regions having a total linearly polarized intensity normalized to the peak value ($PI_{\text{norm}} = PI/PI_{\text{peak}}$) higher than 10^{-2} , 10^{-3} and 10^{-4} , respectively. These values correspond to the first three contours of Fig. A.1. As in Table 3, the corresponding standard deviations are given in a smaller font.

70%. Table A.3 and Table A.4 show even better results at longer wavelengths ($\lambda = 1.3$ mm and $\lambda = 3.0$ mm, respectively). To check whether the polarized emission susceptible to be observed recovers the magnetic field topology, we compute the recovery rates for different levels of total linearly polarized dust emission normalized to the peak ($PI_{\text{norm}} = PI/PI_{\text{peak}}$) at $\lambda = 0.8$ mm. We use the same values of the contour levels of Fig. A.1. We compute the mean recovery rates over all the simulations and projections separated in the same two cases as in Table 3. We find that even for the first contour, that corresponds to the most intense emission and thus the most likely to be detected, the recovery rates are found to be higher than 83% for the moderate magnetic field simulations, and higher than 92% for the less magnetized simulations. As the contour level decreases, the recovery rate increases, consistently with the results of Table 3 seen for larger scales.

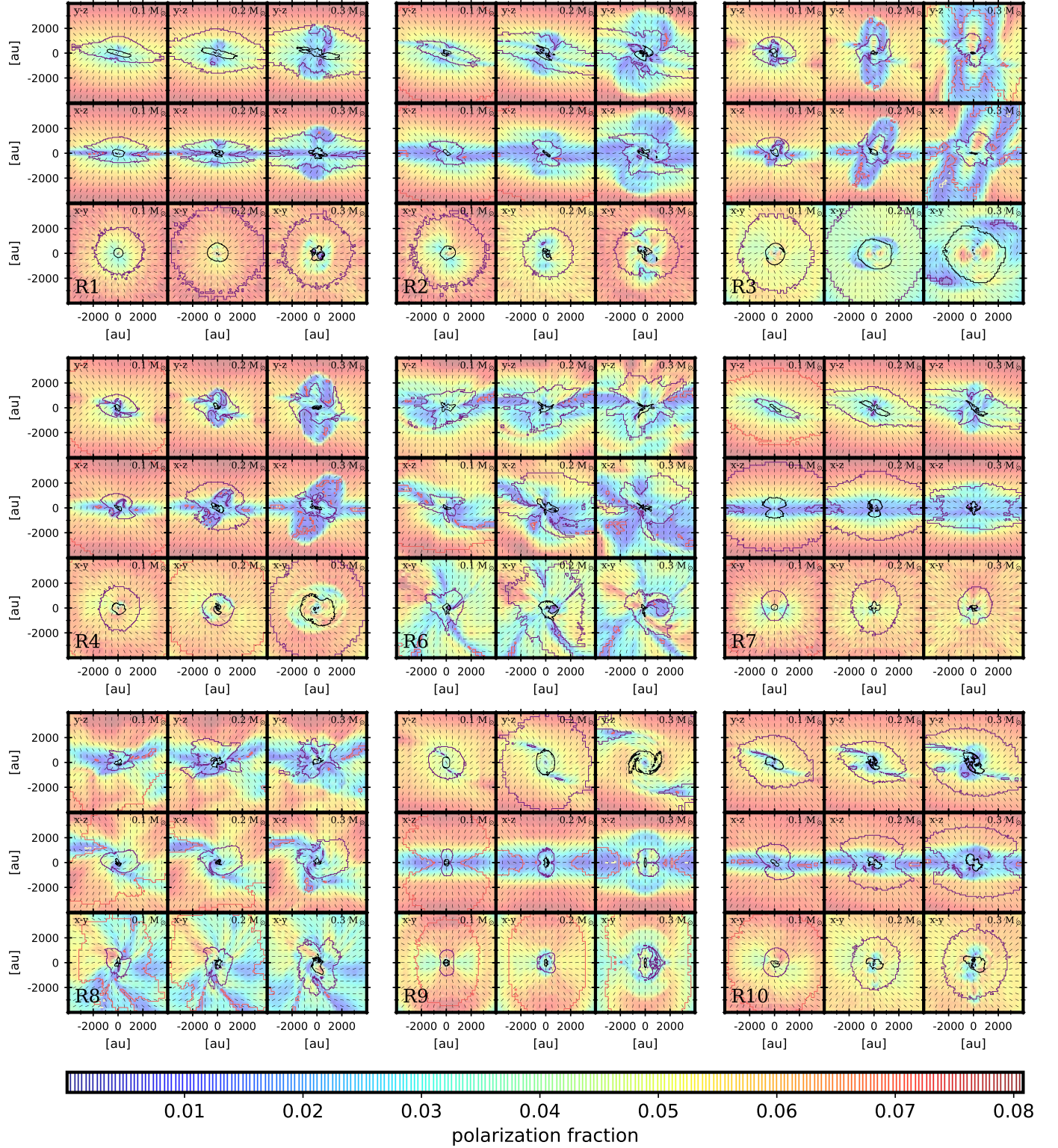


Fig. 8. Results from the synthetic observation at $\lambda = 1.3$ mm showing the polarization fraction (background image), the polarized intensity contours and the inferred magnetic field orientation vectors. The contours correspond to the linearly polarized intensity normalized to the peak value at levels 10^{-2} (black), 10^{-3} (purple), 10^{-4} (red), and 10^{-5} (yellow).

5.1.2. Physical and observational effects responsible for poor measurements in disks and outflows

We now investigate the lines of sight associated to large errors in the reconstructed magnetic field maps, with the goal of identifying the local physical properties responsible for the mismatch.

Since the local gas density and its temperature both scale with radii in protostellar envelopes, we first look for the distribution of inaccurate measurements in function of distance to the central protostellar embryo. Figure 11 shows the percentage of lines of sight that have a discrepancy (expressed in terms of the absolute value of the difference $|\Delta\phi|$) higher or equal to 30° as

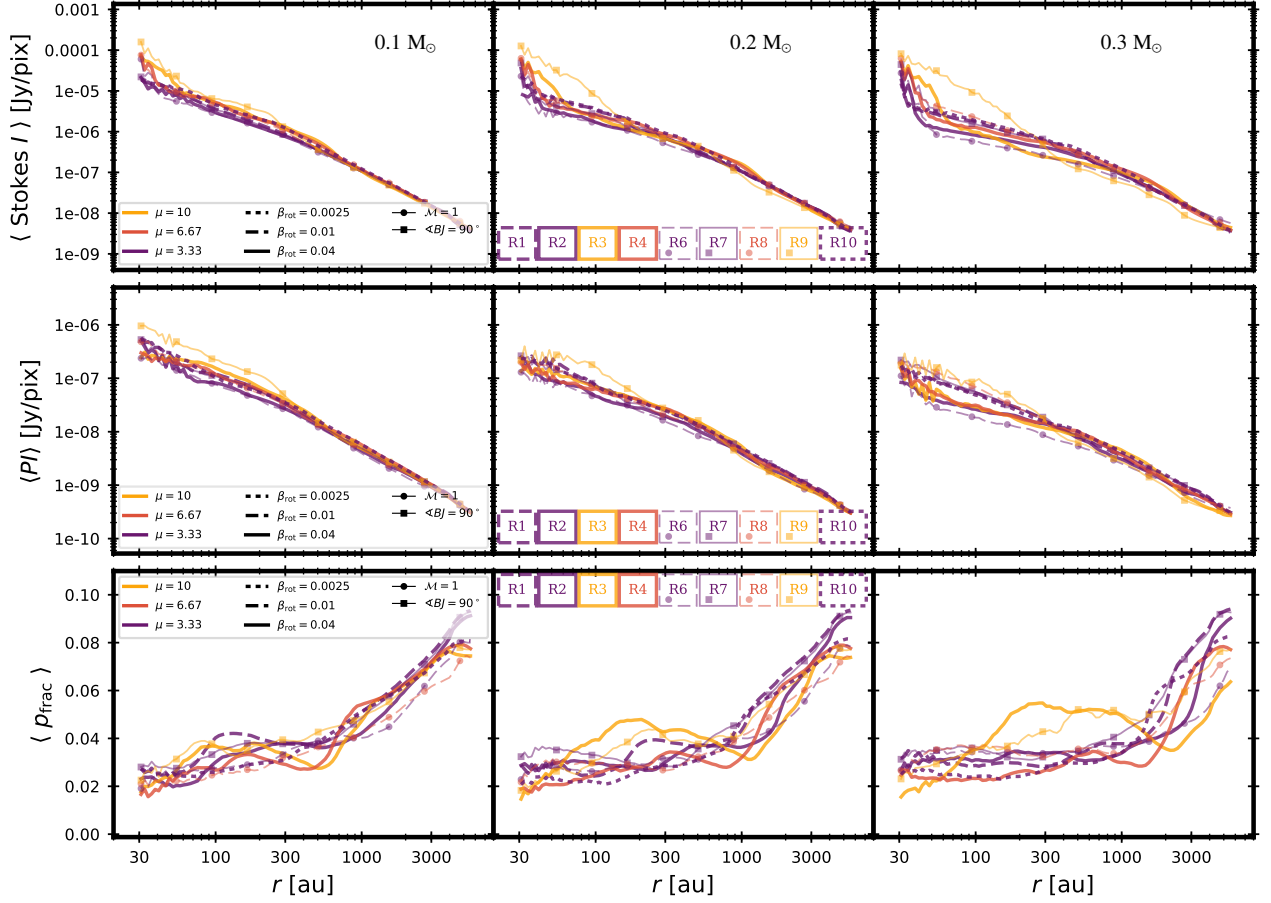


Fig. 9. Radial profiles of the synthetic observation at $\lambda = 1.3$ mm. From top to bottom: total dust emission (Stokes I), total linearly polarized dust emission (PI), and polarization fraction (p_{frac}). From left to right: results at $m_{\text{sink}} = 0.1, 0.2$, and $0.3 M_{\odot}$.

a function of the radius (using 100 logarithmic bins). This figure shows distinctive radial distances at which the points with large discrepancies represent an important contribution. These regions develop outwards in time, diluting this fraction over a larger volume. The more magnetized simulations ($\mu = 3.33$) display percentages higher than 10% over larger regions. Simulations with $\theta = 90^\circ$ start to show regions of high discrepancy at a much larger radius. Once the sinks in the simulations have reached $0.3 M_{\odot}$, most of the simulations show a region of high discrepancy within a distance of 30 – 100 au with respect to the sink position. Even though Figs. 11 and 6 do not seem to display the same behavior, these regions of higher discrepancy seem to be connected to larger levels of disorganization of the field line orientations along the line of sight.

To better understand the role of the intrinsic degree of organization of the magnetic field lines and the reliability of the orientation inferred from dust polarization observations we present in Figs. 12 and 13 2D histograms showing the absolute value of the difference $|\Delta\phi|$ as a function of the circular variance V_ϕ at $\lambda = 1.3$ mm. Analogous results for $\lambda = 0.8$ mm and $\lambda = 3.0$ mm are shown in the Appendix in Figs. A.8 and A.9, and Figs. A.10 and A.11, respectively. All the results correspond to the stacked values for the three projections ($y-z$, $x-z$ and $x-y$) of Fig. A.6 (Fig. A.5 and Fig. A.7 for $\lambda = 0.8$ mm and $\lambda = 3.0$ mm). The contour lines corresponds to the 2D histogram contour levels of the distribution of the lines of sight at 10^5 (yellow), 10^4 (red), 10^3 (purple), and 10^2 (black) counts, while the color coded background displays the mean column density for a given bin of V_ϕ

and $|\Delta\phi|$. We present in Fig. 12 the distribution for the more standard conditions (no initial turbulence and $\theta = 30^\circ$, namely simulations R1, R2, R3, R4 and R10), while Fig. 13 shows the same results but for the simulations including turbulence (R6, R8), or with a rotation axis perpendicular to the initial magnetic field orientation (R7, R9). In both cases the results have been organized by blocks of decreasing level of magnetization (increasing μ), and increasing levels of rotation (increasing values of β_{rot}). In all the simulations most of the points in the map (contours higher or equal to 10^4 counts) are characterized by low levels of $|\Delta\phi|$ (typically $\leq 10^\circ$) and low to moderate values of V_ϕ , with low values of the mean column density. These points corresponds to regions that, other than the hourglass, have not been significantly disturbed by the infall, the turbulence or the outflows and cover a great surface of the maps (yellowish regions of Fig. 4 for example). Figures 12 and 13 show a general behavior for points at low to moderate column densities ($\langle N \rangle \leq 10^{25} \text{ cm}^{-3}$), where the discrepancy between the inferred magnetic field orientation and the actual mean orientation increases with the intrinsic degree of disorganization of the field lines and is consistent with the expected angular dispersion (see Fig. C.1). On the other hand, at higher column densities, the behavior differs from what is expected, displaying $|\Delta\phi|$ values higher than what can be attributed to the dispersion only. Particularly, points with high $|\Delta\phi|$ ($\geq 30^\circ$) and low values of V_ϕ (≤ 0.2) are puzzling, but they remain extremely rare. Even the abundance of points with $|\Delta\phi| > 30^\circ$ and $V_\phi \leq 0.5$ remain extremely low at the three wavelengths (typically less than 0.01%, with only the very particular case of

the simulation R7, projection $y - z$ at $m_{\text{sink}} = 0.3 M_{\odot}$ reaching 0.1%). These points can be only partially explained by a lower efficiency of the grain alignment (see the Appendix B for a comparison with the case of perfectly aligned dust grains), a higher opacity of the layers surrounding the protostar that only allows to recover the foreground information, and a dust temperature gradient, which are not included in the computation of the mean orientation of the magnetic field. To assess whether the opacity is responsible of the lower recovery rates, we stack the maps at $\lambda = 0.8 \text{ mm}$ for all the simulations, timesteps and projections and we compute the recovery rate in three opacity ranges. For all the lines of sight with $\tau_{0.8 \text{ mm}} \geq 1$ we obtain a recovery rate of only 42.5%. For $\tau_{0.8 \text{ mm}}$ in the range $0.1 - 1$, we obtain a recovery rate of 79.4%, while for $\tau_{0.8 \text{ mm}}$ in the range $0.01 - 0.1$ the recovery rate reaches 81.7%. This clearly shows that the reconstructed B -fields of regions with high column densities most likely suffer from opacity effects, and that these regions might benefit from multi-wavelength observations.

Figure 12 suggests that, in otherwise similar initial conditions ($\beta = 0.04$, $M = 0$, $\theta = 30^\circ$), the more magnetized case (R2) has initially (at $m_{\text{sink}} = 0.1 M_{\odot}$) higher levels of $|\Delta\phi|$, but as the simulations evolve, the overall levels of discrepancy become comparable (similar contour levels). Nevertheless, the most puzzling measurements being the sight lines where the magnetic field is relatively well organized (low variance), but displaying large discrepancies (high $|\Delta\phi|$) are more important for the less magnetized simulation (R3) at all evolutionary stages (shown in Fig. 12) and they are mostly associated to high column density lines of sight corresponding to the very small radii (disk scales), where radiative transfer effects cannot be easily neglected, even at millimeter wavelengths.

For the non-standard configurations shown in Fig. 13, those including turbulence show relatively similar levels of discrepancy (simulations R6 and R8), indicating that the relative importance of the magnetization level is reduced in the presence of turbulence. Nevertheless, the presence of turbulence does not seem to be the main culprit of the low recovery rates. For instance, Table A.2 shows that simulations R1 and R6 display similar recovery rates, within the error bar, at different scales.

On the other hand, simulations with $\theta = 90^\circ$ (R7 and R9) show an increased importance of the magnetization level. Simulation R9 (the less magnetized one) exhibits a quite peculiar behavior, where although the overall $|\Delta\phi|$ values remain low, it develops a region where the discrepancy is maximal (even for values of V_ϕ lower than 0.2), reaching values closer to 90° .

Figure 12 also shows that the accuracy of polarized dust emission maps in tracing the magnetic field topology in protostars has weak and rather unclear dependence on the initial values of the rotational energy β_{rot} in the more magnetized case ($\mu = 3.33$, first three rows), displaying overall a larger level of discrepancy between the intrinsic magnetic field mean orientation and the reconstructed orientation from the polarized dust emission for the simulation with larger rotational energy (R2), and the lowest one for the simulation with intermediate rotational energy level (R1).

5.2. Depolarization and magnetic field organization

Finally, to better understand the influence of the magnetic field topology on the polarization fraction, we compare the distribution of the polarization fraction (p_{frac}) as a function of the circular variance (V_ϕ) obtained for our synthetic maps to a test case. In the case of our synthetic maps, the alignment has been computed according to the B-RAT theory, including the imperfect internal alignment and the imperfect Davis-

Greenstein mechanisms, as described in Sect. 2.4.3 (top row of Fig. 14, labeled as B-RAT+II+IDG), while for the test case the alignment is imposed in such a manner that all the dust grains susceptible to align are perfectly aligned with the B -field lines (bottom row of Fig. 14, labeled as PA). In Fig. 14 we show 2D histograms of p_{frac} vs V_ϕ by stacking the results of all the simulations, time-steps and projections, at three wavelengths. This figure shows a clear anti-correlation between these two quantities, indicating that the degree of polarization decreases with an increasing level of disorganization of the magnetic field along the line-of-sight, consistent with the anticorrelation between the polarization fraction and the dispersion of the position angles found in ALMA observations of Class 0 objects (Le Gouellec et al. 2020).

The fact that both cases display the same behavior, supports the idea that a geometrically depolarized signal due to the non-organized component of the magnetic field might be greatly responsible for the lower levels of polarization observed in denser regions down to the scales of protostellar envelopes, in agreement with observations at larger scales (Doi et al. 2020; Planck Collaboration et al. 2015b,a). However, while at large scales the turbulence of the gas may be at the main physical cause of the magnetic field disorganization, inside protostellar cores it seems the gravitational field and the launching of protostellar outflows are more likely culprit, as models with turbulence don't show significantly more disorganized B -field, nor poorer fidelity, than models without, as shown in Table A.2.

5.3. Significance of other polarization-producing processes in protostellar envelopes

Our analysis relies on the hypothesis that dust grains align with the local magnetic field, imperfectly, in proportion that is related to local radiation conditions (B-RATs) and grain properties. Dedicated studies of other physical effects producing polarization of the dust thermal emission, along with better dust models, are necessary to shed light on the precise conditions in which polarization seen at millimeter wavelengths could trace other processes. However, here we reinforce our hypothesis by recalling a few of them and give simple qualitative arguments as of why they are not expected to be dominating in typical conditions reigning in protostellar envelopes.

While at the protostar disk scales the alignment of dust grains with local magnetic field lines can become more difficult to realize, due to the higher rate of collisions (Tazaki et al. 2017), the gaseous damping timescale is inversely proportional to gas density and gas temperatures. Hence, such loss of efficiency is not expected in protostellar envelopes where densities are lower than 10^6 cm^{-3} and temperatures are quite low ($T < 20 \text{ K}$). It has also been suggested that in conditions of high opacity and anisotropic radiation field, usually met in disks, the dust self-scattering of the radiation field from large grains ($\sim 100 \mu\text{m}$) could dominate the polarized signal at mm wavelengths (Kataoka et al. 2015, 2017, see also Kirchschlager & Bertrang 2020; Brunngräber & Wolf 2020). Despite the indications of large grains at the protostellar scales probed in our analysis, not only the conditions are not met to produce significant polarization from self-scattering, but the levels of observed polarization in embedded protostars (a few percent to a few tens of percent) cannot be produced with self-scattering polarization.

A highly anisotropic radiation field could reduce the radiative precession time-scale to values shorter than the Larmor time-scale, inducing a polarization of dust thermal emission due

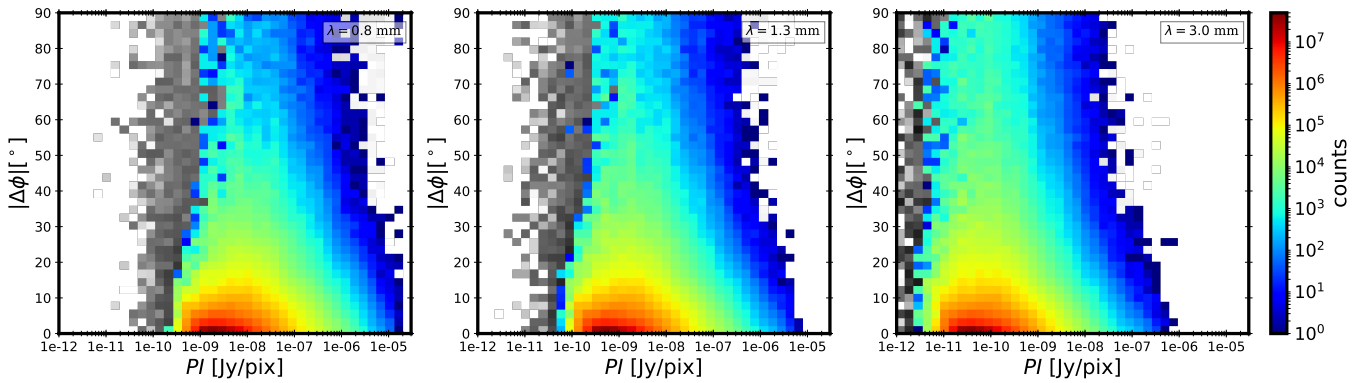


Fig. 10. 2D histograms of the discrepancy between the mean B -field orientation and the orientation inferred from the polarized dust emission, and the intensity of the polarized dust emission at three wavelengths. From left to right $\lambda = 0.8$, 1.3, and 3.0 mm. Each histogram has been constructed using the data stacked for all simulations, time-steps and projections. The color histograms show the results using only the lines of sight that have a polarization fraction above 1%, while the grayscale part corresponds to the rest of the points.

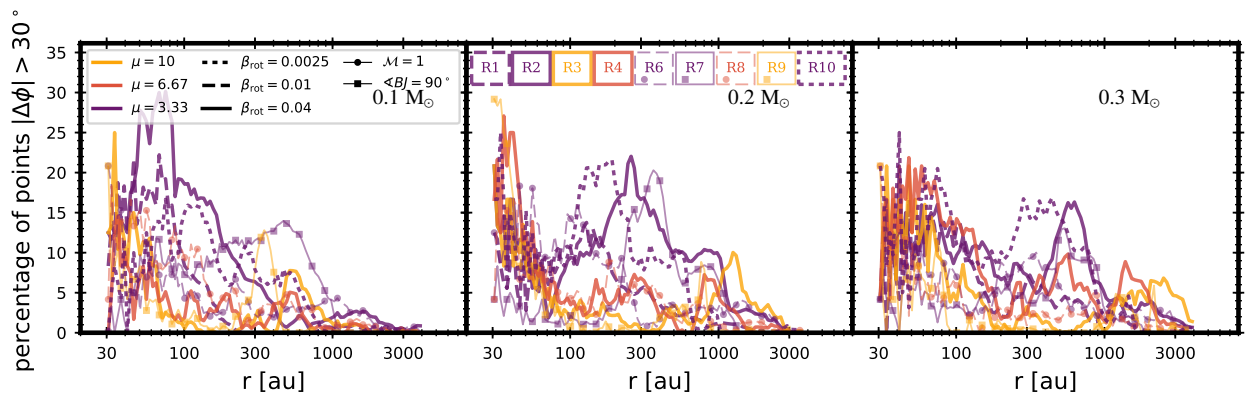


Fig. 11. Percentage of pixels with $|\Delta\phi| > 30^\circ$ at $\lambda = 1.3$ mm in logarithmic radial bins.

to the k-RAT mechanism, related to the radiation anisotropy and not to the magnetic field. This mechanism is favored for the large grains (for a discussion, see for example the work of Pattle et al. 2021 in the Orion Source I), and necessitate extremely irradiated conditions at the wavelengths similar to the dust grain sizes, which are not the ones typical of embedded low-mass protostars (Le Gouellec et al. in prep).

Finally, mechanical alignment of dust grains with the local gas flow has been proposed as an extra mechanism to produce polarized dust emission from irregular grains (Hoang et al. 2018), with a rotation axis parallel to the velocity drift direction. While this mechanism could in principle be at work for example around massive protostars where radiative pressure drives the outflow (Mignon-Risse et al. 2021), its conditions seem very sensitive to the flow properties (high velocities to enhance the alignment efficiency, but not as high as to disrupt the dust grains) and quite unable to explain the large range of observations showing polarized dust emission in protostars. We also stress that no convincing observational signature of such alignment process was yet found in protostellar environments (Cortes et al. 2021; Aso et al. 2021).

6. Conclusions

In this paper, we present a thorough investigation of the fidelity and limitations of using dust polarized emission as a tracer of the magnetic field topologies in the dense regions of protostellar cores forming solar type stars. Our concerns were mostly

focused on quantifying the errors induced by (i) widely varying physical conditions along each individual line of sight used to probe the dust grain emission of the protostellar objects, and (ii) its potentially devastating combination with the averaging effects of complex B -field line orientations along those same lines of sight.

To assess the importance of these effects, we have performed the analysis of magnetic field properties in 27 realizations of MHD models following the evolution of physical properties in star-forming cores. Assuming a uniform population of oblate dust grains which sizes follow the standard MRN, we produced synthetic polarized dust emission maps for dust grains aligned with the local B -field thanks to B-RATs mechanism. We provide a detailed comparison of these synthetic maps and their relative models.

We find that, in most cases, (sub-)millimeter polarized dust emission is a robust tracer of the magnetic field topologies in inner protostellar envelopes and is successful at capturing the details of the magnetic field spatial distribution down to radii ~ 100 au. Measurements of the line-of-sight averaged magnetic field line orientation using the polarized dust emission are precise to $< 15^\circ$ (typical of the error on polarization angles obtained with observations from large mm polarimetric facilities such as ALMA) in about 95% of the independent lines of sight peering through protostellar envelopes at all radii. When focusing on the smaller envelope radii < 500 au, where the magnetic field lines are more likely perturbed from the initially smooth configuration

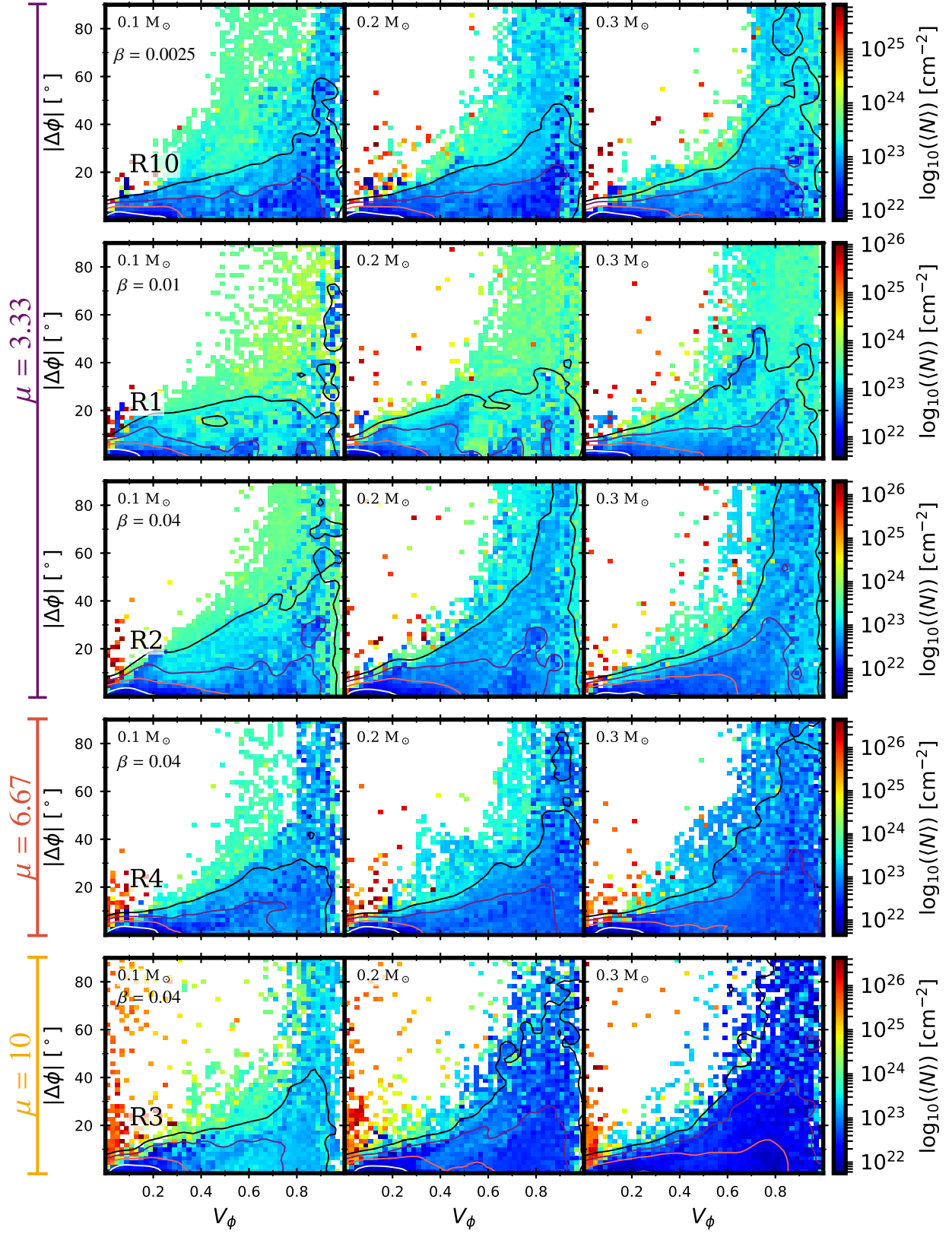


Fig. 12. Distribution of the discrepancy between the B angle inferred from the synthetic polarized dust emission at $\lambda = 1.3$ mm and the mean orientation of the B lines in the simulation as a function of the circular variance V_ϕ for the simulations with standard conditions. All these simulations do not include any initial turbulence ($M = 0$) and have an initial inclination angle between the initial rotation axis and the magnetic field θ of 30° . The contour lines show the smoothed 2D histogram contour levels at 10^5 (yellow), 10^4 (red), 10^3 (purple), and 10^2 (black) counts. The color coded background corresponds to the mean column density.

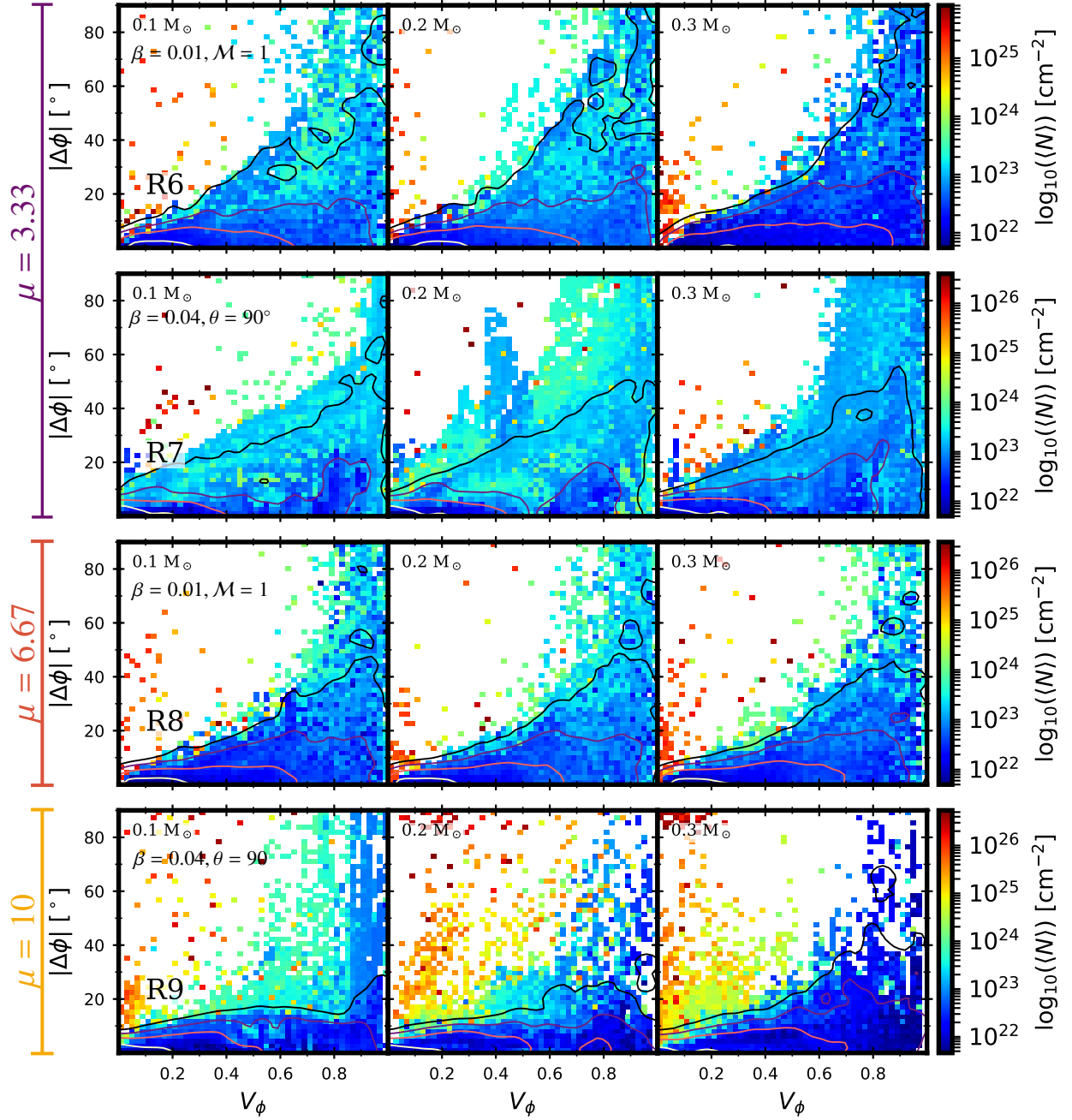


Fig. 13. Distribution of $|\Delta\phi|$ at $\lambda = 1.3$ mm as a function of the circular variance V_ϕ for the simulations with non standard conditions. The contours and the background image are the same of Fig. 12. Simulations R6 and R8 include turbulence ($M = 1$), while the simulations R7 and R9 have an initial angle between the rotation axis and the magnetic field axis of $\theta = 90^\circ$.

by infall and outflow, 75% of the lines of sight still give robust results.

Large discrepancies between the integrated B -field mean orientation and the orientation reconstructed from the polarized dust emission are mostly observed in lines of sight probing large column densities. Our analysis shows that, at disk scales, physical conditions producing high opacity of the thermal dust emission are mostly responsible for the small fraction of mediocre measurements (inaccuracy of 50% or more on the recovered B -field position angle at opacities higher than 1 mag). While the use of longer wavelengths performs slightly better at recovering the true orientation of the magnetic fields, our study suggest that,

at those scales, most measurements of magnetic field lines orientation will suffer from large ($> 30^\circ$) error bars. Discrepancy is also found associated to a small fraction of lines of sight where the magnetic field is highly disorganized, such as outflow cavity walls and accretion shocks: in such lines of sight the concept of integrated B -field mean orientation does not make sense, and no good measurement can therefore be done. We find that the polarization fraction is correlated to the degree of organization of the magnetic field along the line of sight, confirming that the behavior observed at larger scales, in less dense gas, holds true down to the scales of the envelopes of protostars. Hence, low levels of

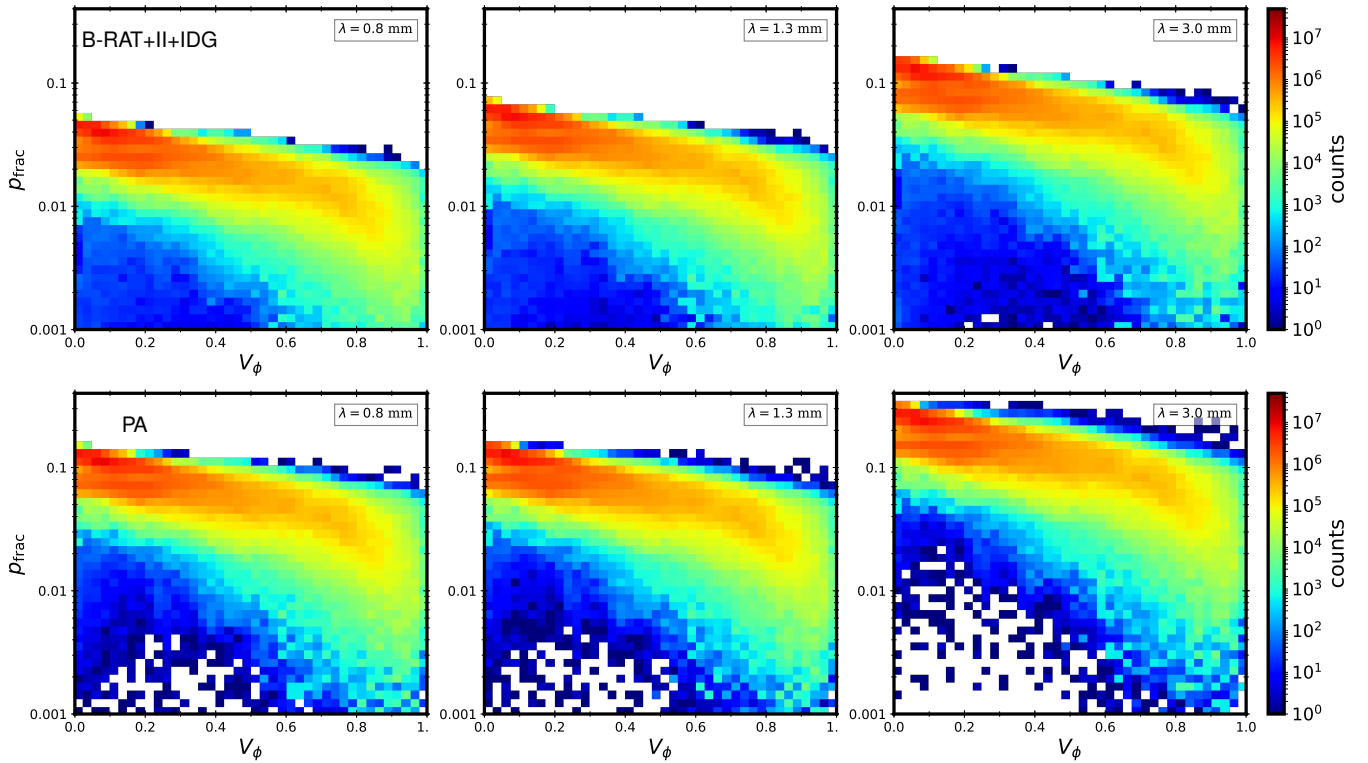


Fig. 14. 2D histograms of the polarization fraction as a function of the circular variance for all the stacked maps at three wavelengths (from left to right $\lambda = 0.8, 1.3$ and 3.0 mm). The top row show the results for the case where the alignment is computed according to the B-RAT theory along with the II and IDG mechanisms (B-RAT+II+IDG), as described in Section 2.4.3, while the bottom row shows the results for the case where dust grains are supposed perfectly aligned (PA) with the magnetic field.

polarization fraction in the observations could be used as a flag to avoid these measurements affected by large errors.

Acknowledgements. This research has received funding from the European Research Council (ERC) under the European Union’s Horizon 2020 research and innovation programme (MagneticYSOS project, Grant Agreement No 679937).

References

- Andersson, B.-G., Lazarian, A., & Vaillancourt, J. E. 2015, *ARA&A*, 53, 501
Aso, Y., Kwon, W., Hirano, N., et al. 2021, *ApJ*, 920, 71
Barnett, S. J. 1915, *Physical Review*, 6, 239
Bate, M. R., Bonnell, I. A., & Price, N. M. 1995, *MNRAS*, 277, 362
Bleuler, A. & Teyssier, R. 2014, *MNRAS*, 445, 4015
Brunngräber, R. & Wolf, S. 2020, *A&A*, 640, A122
Cortes, P. C., Le Gouellec, V. J. M., Hull, C. L. H., et al. 2021, *ApJ*, 907, 94
Davis, Leverett, J. & Greenstein, J. L. 1951a, *ApJ*, 114, 206
Davis, Jr., L. & Greenstein, J. L. 1951b, *ApJ*, 114, 206
Doi, Y., Hasegawa, T., Furuya, R. S., et al. 2020, *ApJ*, 899, 28
Dolginov, A. Z. & Mitrofanov, I. G. 1976, *Ap&SS*, 43, 291
Draine, B. T. 1996, in *Astronomical Society of the Pacific Conference Series*, Vol. 97, *Polarimetry of the Interstellar Medium*, ed. W. G. Roberge & D. C. B. Whittet, 16
Draine, B. T. & Flatau, P. J. 2000, *DDSCAT: The discrete dipole approximation for scattering and absorption of light by irregular particles*
Fromang, S., Hennebelle, P., & Teyssier, R. 2006, *A&A*, 457, 371
Galametz, M., Maury, A., Girart, J. M., et al. 2020, *A&A*, 644, A47
Galli, D. & Shu, F. H. 1993, *ApJ*, 417, 243
Gold, T. 1952, *MNRAS*, 112, 215
Hennebelle, P. & Ciardi, A. 2009, *A&A*, 506, L29
Hennebelle, P., Commerçon, B., Chabrier, G., & Marchand, P. 2016, *ApJ*, 830, L8
Hennebelle, P., Commerçon, B., Lee, Y.-N., & Charnoz, S. 2020, *A&A*, 635, A67
Herranen, J., Lazarian, A., & Hoang, T. 2021, *ApJ*, 913, 63
Hildebrand, R. H. & Dragovan, M. 1995, *ApJ*, 450, 663
Hoang, T., Cho, J., & Lazarian, A. 2018, *ApJ*, 852, 129
Hoang, T. & Lazarian, A. 2014, *MNRAS*, 438, 680
Hoang, T. & Lazarian, A. 2016, *ApJ*, 831, 159
Jones, R. V. & Spitzer, Jr., L. 1967, *ApJ*, 147, 943
Jones, T. A. & James, W. R. 1969, *Journal of the International Association for Mathematical Geology*, 1, 129
Joos, M., Hennebelle, P., & Ciardi, A. 2012, *A&A*, 543, A128
Kataoka, A., Muto, T., Momose, M., et al. 2015, *ApJ*, 809, 78
Kataoka, A., Tsukagoshi, T., Pohl, A., et al. 2017, *ApJ*, 844, L5
Kirchschlager, F. & Bertrang, G. H. M. 2020, *A&A*, 638, A116
Krasnopolsky, R., Li, Z.-Y., Shang, H., & Zhao, B. 2012, *ApJ*, 757, 77
Landi Degl’Innocenti, E. & Landolfi, M. 2004, *Polarization in Spectral Lines*, Vol. 307
Lazarian, A. & Hoang, T. 2007a, *MNRAS*, 378, 910
Lazarian, A. & Hoang, T. 2007b, *ApJ*, 669, L77
Le Gouellec, V. J. M., Maury, A. J., Guillet, V., et al. 2020, *A&A*, 644, A11
Li, A. & Draine, B. T. 2001, *ApJ*, 554, 778
Li, Z.-Y., Banerjee, R., Pudritz, R. E., et al. 2014, *Protostars and Planets VI*, 173
Li, Z.-Y. & Shu, F. H. 1996, *ApJ*, 472, 211
Machida, M. N., Inutsuka, S.-i., & Matsumoto, T. 2014, *MNRAS*, 438, 2278
Mardia, K. V. 1975, *Journal of the Royal Statistical Society: Series B (Methodological)*, 37, 349
Martínez González, M. J., Manso Sainz, R., Asensio Ramos, A., & Belluzzi, L. 2011, *Monthly Notices of the Royal Astronomical Society*, 419, 153
Masson, J., Chabrier, G., Hennebelle, P., Vaytet, N., & Commerçon, B. 2016, *A&A*, 587, A32
Mathis, J. S., Mezger, P. G., & Panagia, N. 1983, *A&A*, 128, 212
Mathis, J. S., Rumpl, W., & Nordsieck, K. H. 1977, *ApJ*, 217, 425
Matsumoto, T., Machida, M. N., & Inutsuka, S.-i. 2017, *ApJ*, 839, 69
Mignon-Risse, R., González, M., & Commerçon, B. 2021, *A&A*, 656, A85
Mouschovias, T. C. & Ciolek, G. E. 1999, in *NATO Advanced Study Institute (ASI) Series C, Vol. 540, The Origin of Stars and Planetary Systems*, ed. C. J. Lada & N. D. Kylafis, 305
Pattle, K., Lai, S.-P., Wright, M., et al. 2021, *MNRAS*, 503, 3414
Planck Collaboration, Ade, P. A. R., Aghanim, N., et al. 2015a, *A&A*, 576, A105
Planck Collaboration, Ade, P. A. R., Aghanim, N., et al. 2015b, *A&A*, 576, A104
Purcell, E. M. 1979, *ApJ*, 231, 404
Reissl, S., Seifried, D., Wolf, S., Banerjee, R., & Klessen, R. S. 2017, *A&A*, 603, A71
Reissl, S., Wolf, S., & Brauer, R. 2016, *A&A*, 593, A87

- Roberge, W. G. 2004, in ASP Conf. Series, Vol. 309, Astrophysics of Dust, ed. A. N. Witt, G. C. Clayton, & B. T. Draine, 467
- Seifried, D., Banerjee, R., Klessen, R. S., Duffin, D., & Pudritz, R. E. 2011, MNRAS, 417, 1054
- Spitzer, Jr., L. & McGlynn, T. A. 1979, ApJ, 231, 417
- Tazaki, R., Lazarian, A., & Nomura, H. 2017, ApJ, 839, 56
- Teyssier, R. 2002, A&A, 385, 337
- Valdivia, V., Maury, A., Brauer, R., et al. 2019, MNRAS, 488, 4897

Appendix A: Additional material

In this section we provide complementary material on synthetic observations and their comparisons to properties measured from the models. Figures A.1 and A.2 show the maps from the synthetic observations of the polarized dust emission of the 27 models, at $\lambda = 0.8$ and 3.0 mm. Figures A.3 and A.4 show the azimuthally-averaged profiles of the total dust emission flux density, linearly polarized flux density and the polarization fraction (averaged for the three projections) at $\lambda = 0.8$, and 3.0 mm, respectively.

Figures A.5, A.6 and A.7 are maps of the difference in measured mean B -field orientation, between the model value and the value inferred from the polarized dust emission at $\lambda = 0.8$, 1.3 and 3.0 mm. It shows mostly small differences (light colors or white), and highlights in dark colors the regions where the B -field orientation inferred from the polarized dust emission is very different from the mean magnetic field orientation.

Figures A.8 and A.9 (Figures A.10 and A.11) show the distribution of the discrepancy between the inferred orientation of the magnetic field and the true mean orientation at $\lambda = 0.8$ mm ($\lambda = 3.0$ mm) for the simulations with standard conditions and the ones starting from less prototypical conditions (either $\mathcal{M} = 1$ or $\theta = 90^\circ$), respectively.

Table A.1 gives the detailed recovery rates at $\lambda = 0.8$ for all the simulations (ID), projections (los) and evolutionary stages (m_{sink}) at different scales. The fourth column shows the recovery rate over the whole map, while columns 5, 6 and 7 correspond to the recovery rate in concentric rings of radial distances comprised in the interval given in the header of the table.

We verify the influence of the presence of turbulence on Table A.2. This table shows the mean recovery rates for simulations R1 and R6. These two otherwise identical simulations ($\mu = 3.33$, $\beta_{\text{rot}} = 0.01$ and $\theta = 30^\circ$) differing only on the degree of turbulence (R6 has $\mathcal{M} = 1$) show that the degree of turbulence does not have a strong impact on the recovery rate.

Finally, Tables A.3 and A.4 show the mean recovery rates separated into two cases (moderate and low magnetization degree) similar to Table 3, but at $\lambda = 1.3$, and 3.0 mm, respectively.

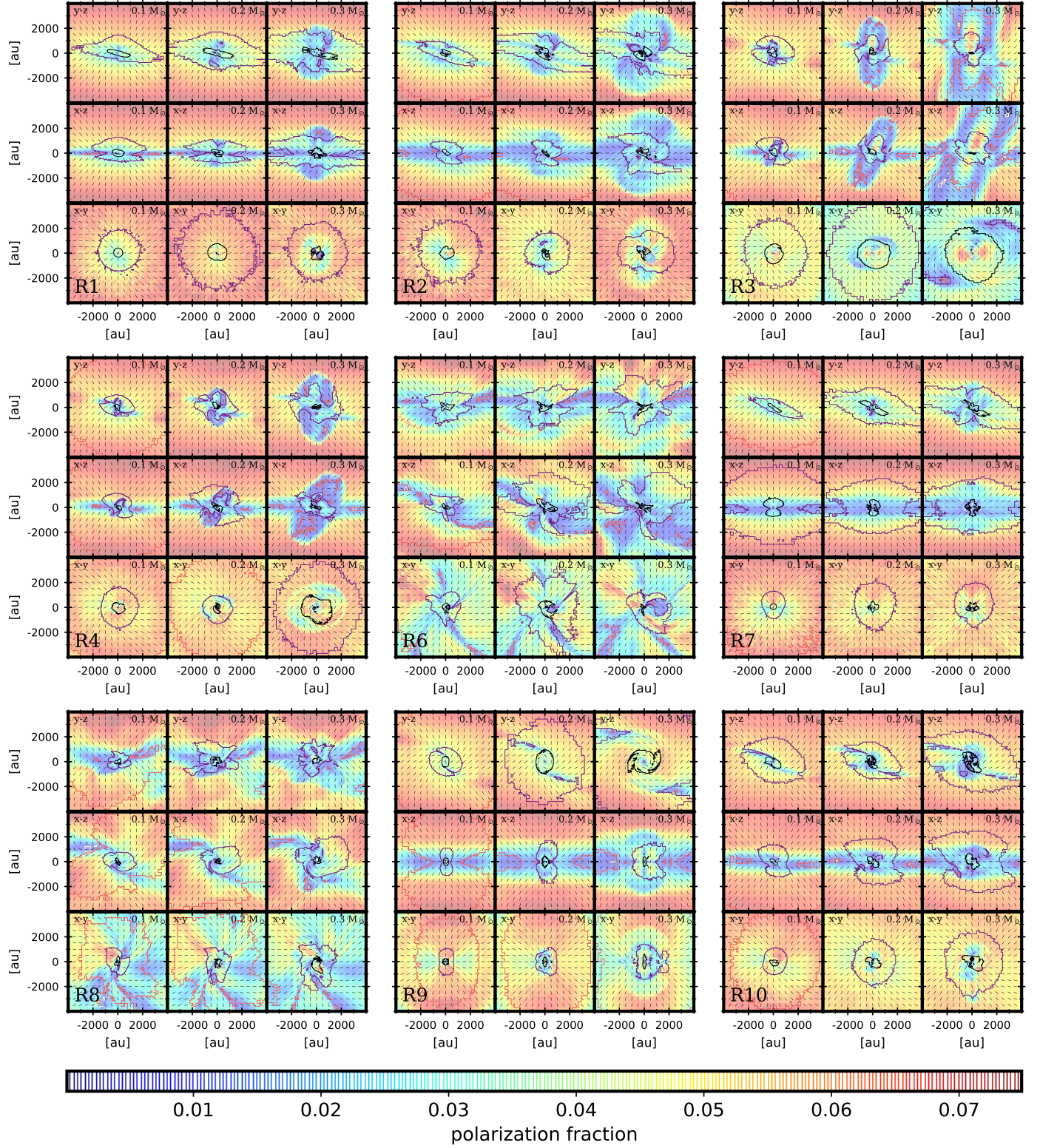


Fig. A.1. Results from the synthetic observation at $\lambda = 0.8$ mm showing the polarization fraction (background image), the polarized intensity contours and the inferred magnetic field orientation vectors. The contours correspond to the linearly polarized intensity normalized to the peak value at levels 10^{-2} (black), 10^{-3} (purple), 10^{-4} (red), and 10^{-5} (yellow).

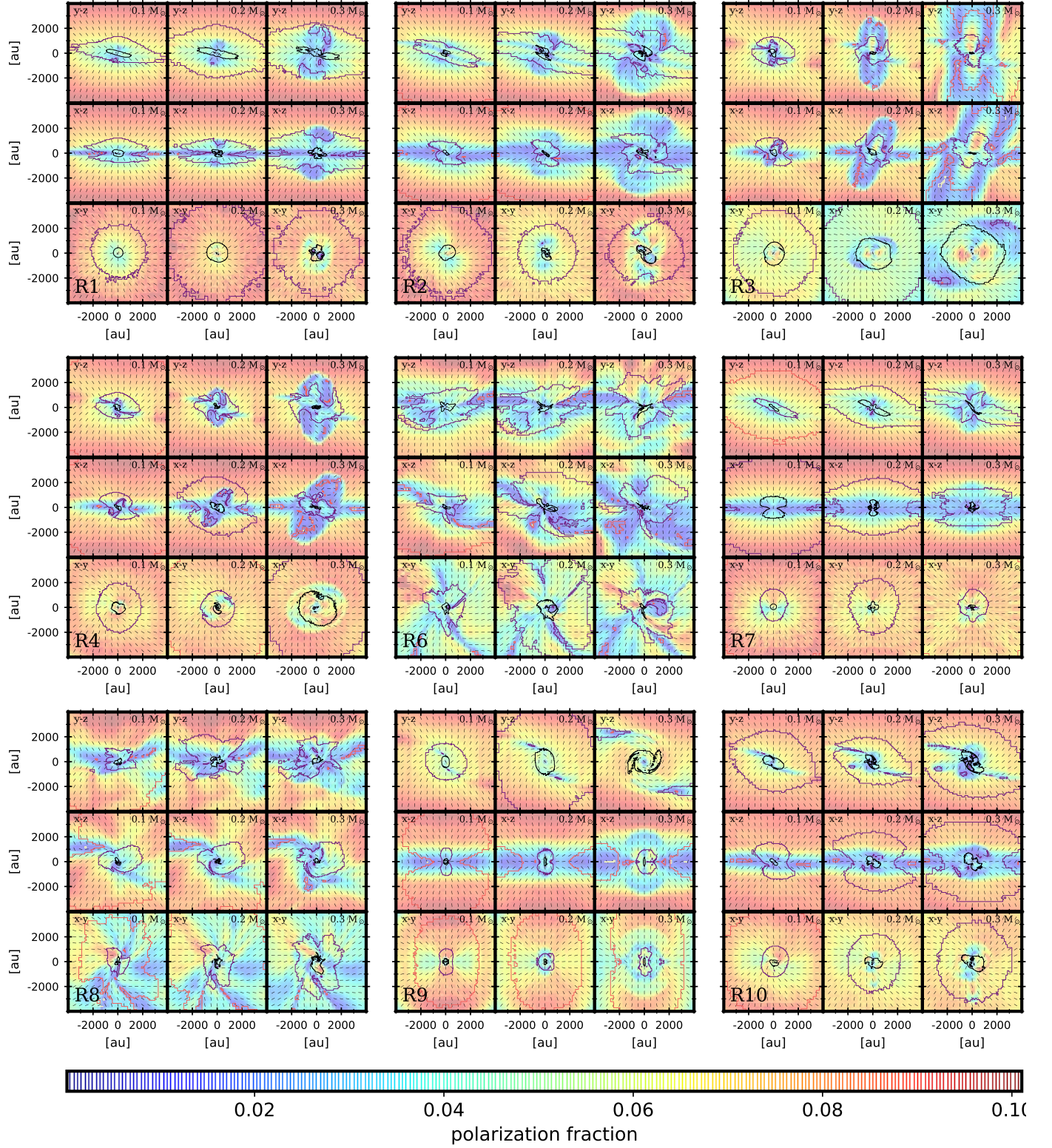


Fig. A.2. Results from the synthetic observation at $\lambda = 3.0$ mm showing the polarization fraction (background image), the polarized intensity contours and the inferred magnetic field orientation vectors. The contours correspond to the linearly polarized intensity normalized to the peak value at levels 10^{-2} (black), 10^{-3} (purple), 10^{-4} (red), and 10^{-5} (yellow).

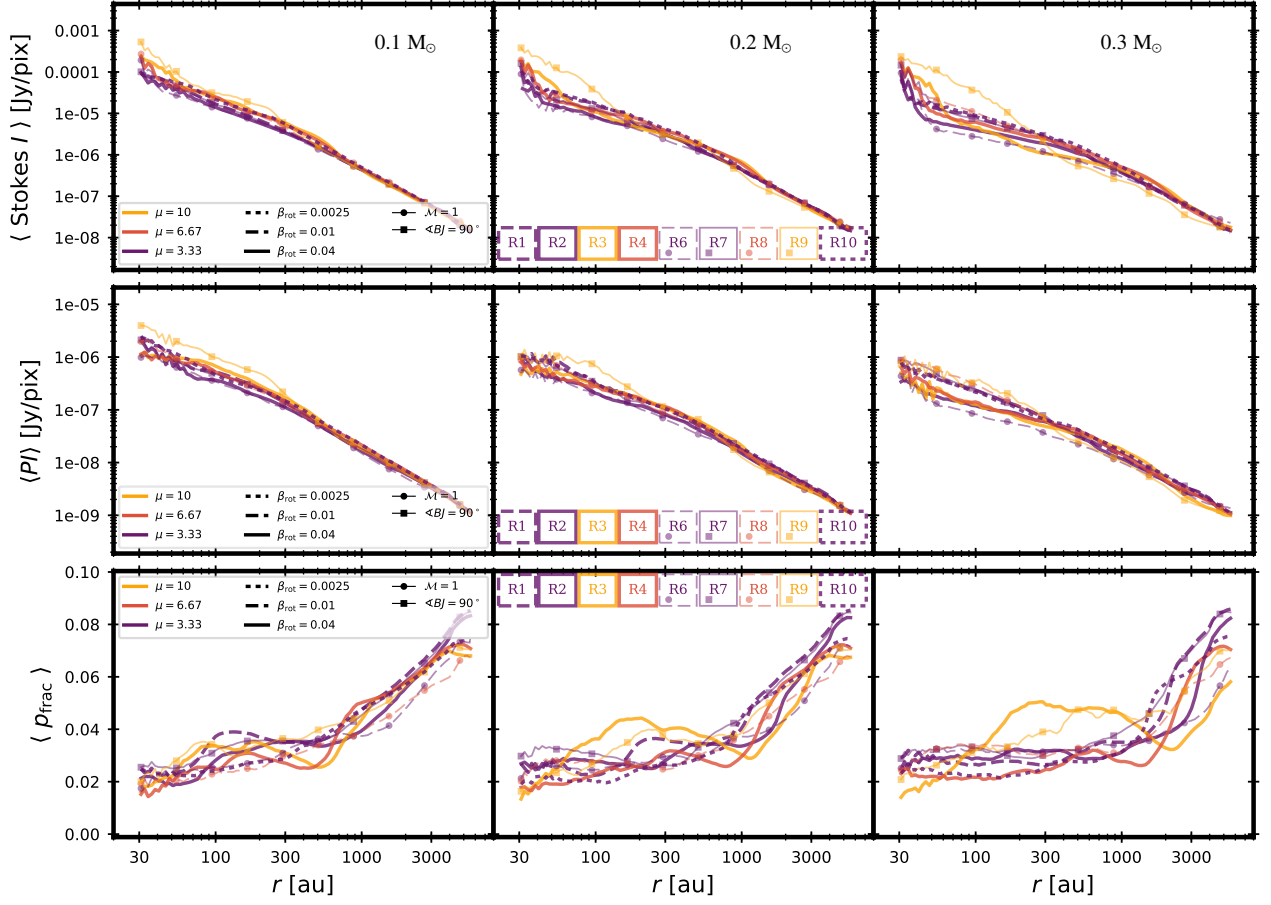


Fig. A.3. Radial profiles of the synthetic observation at $\lambda = 0.8$ mm. From top to bottom: total dust emission (Stokes I), total linearly polarized dust emission (PI), and polarization fraction (p_{frac}).

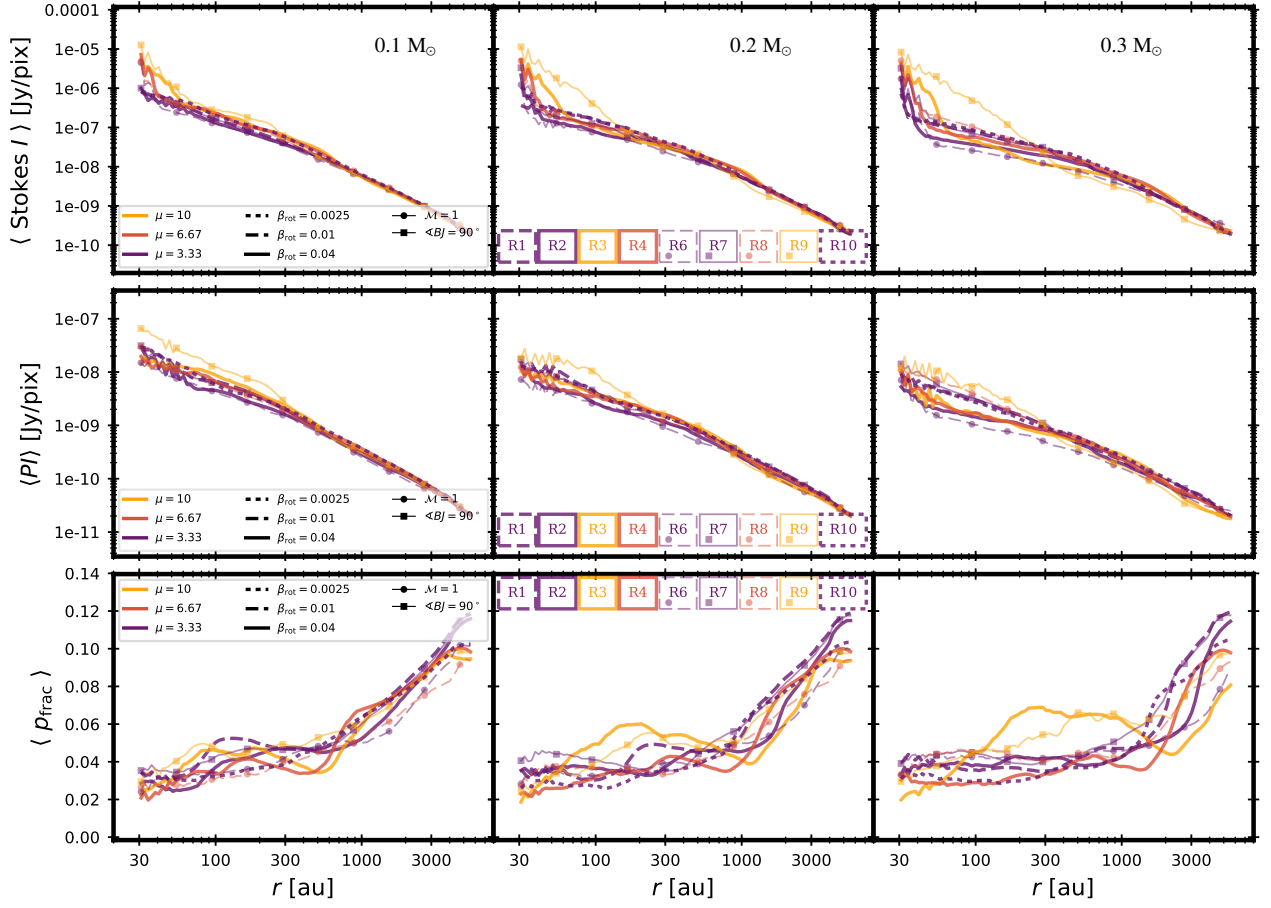


Fig. A.4. Radial profiles of the synthetic observation at $\lambda = 3.0$ mm. From top to bottom: total dust emission (Stokes I), total linearly polarized dust emission (PI), and polarization fraction (p_{frac}).

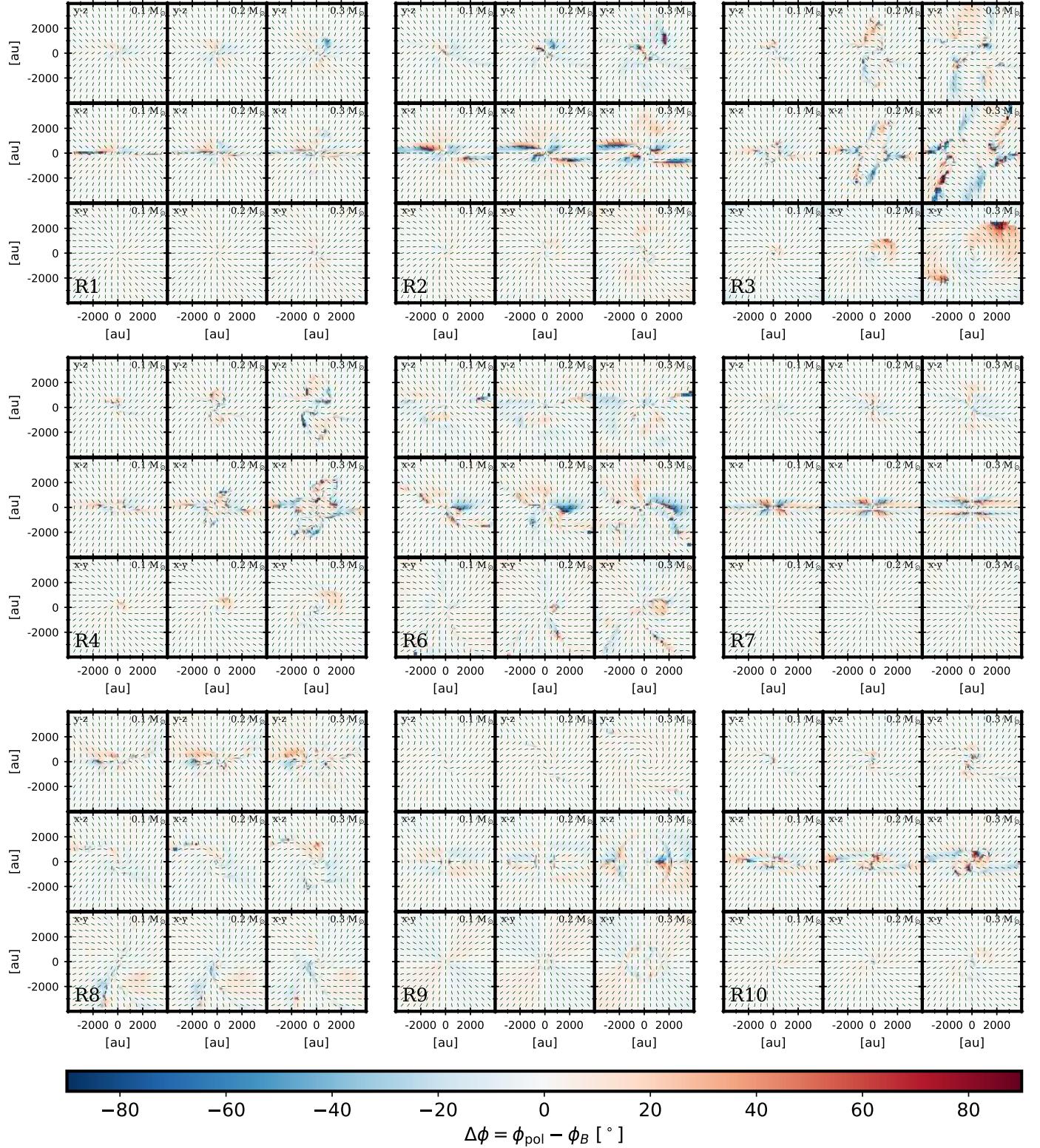


Fig. A.5. Difference maps $\Delta\phi$ at $\lambda = 0.8$ mm. The simulation identifier is shown on the bottom left corner of each block, while the projection and evolutionary step (given by the sink mass) are indicated on the top of each individual map.

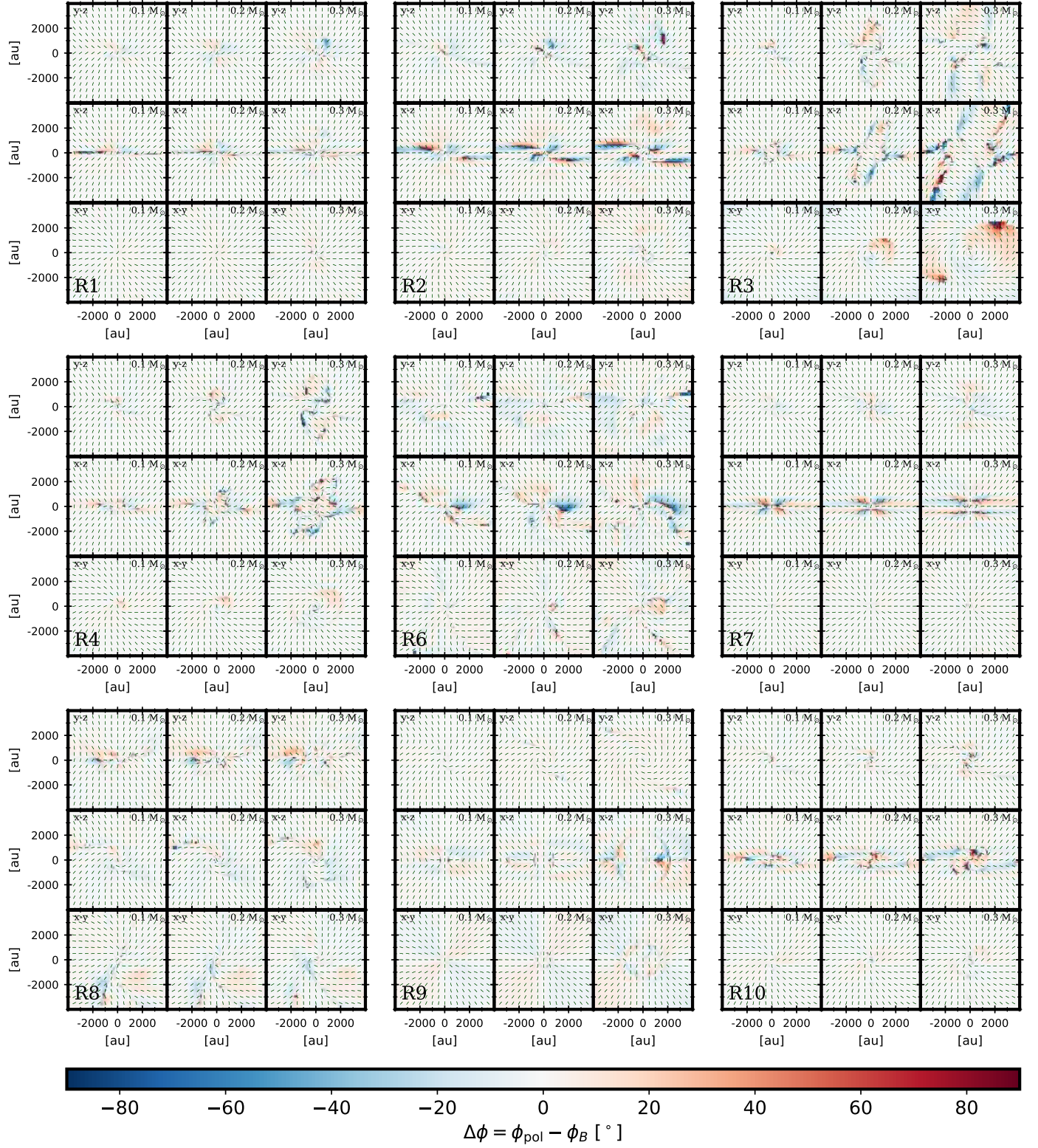


Fig. A.6. Difference maps $\Delta\phi$ at $\lambda = 1.3$ mm. The structure of the figure is the same than for Fig. A.5.

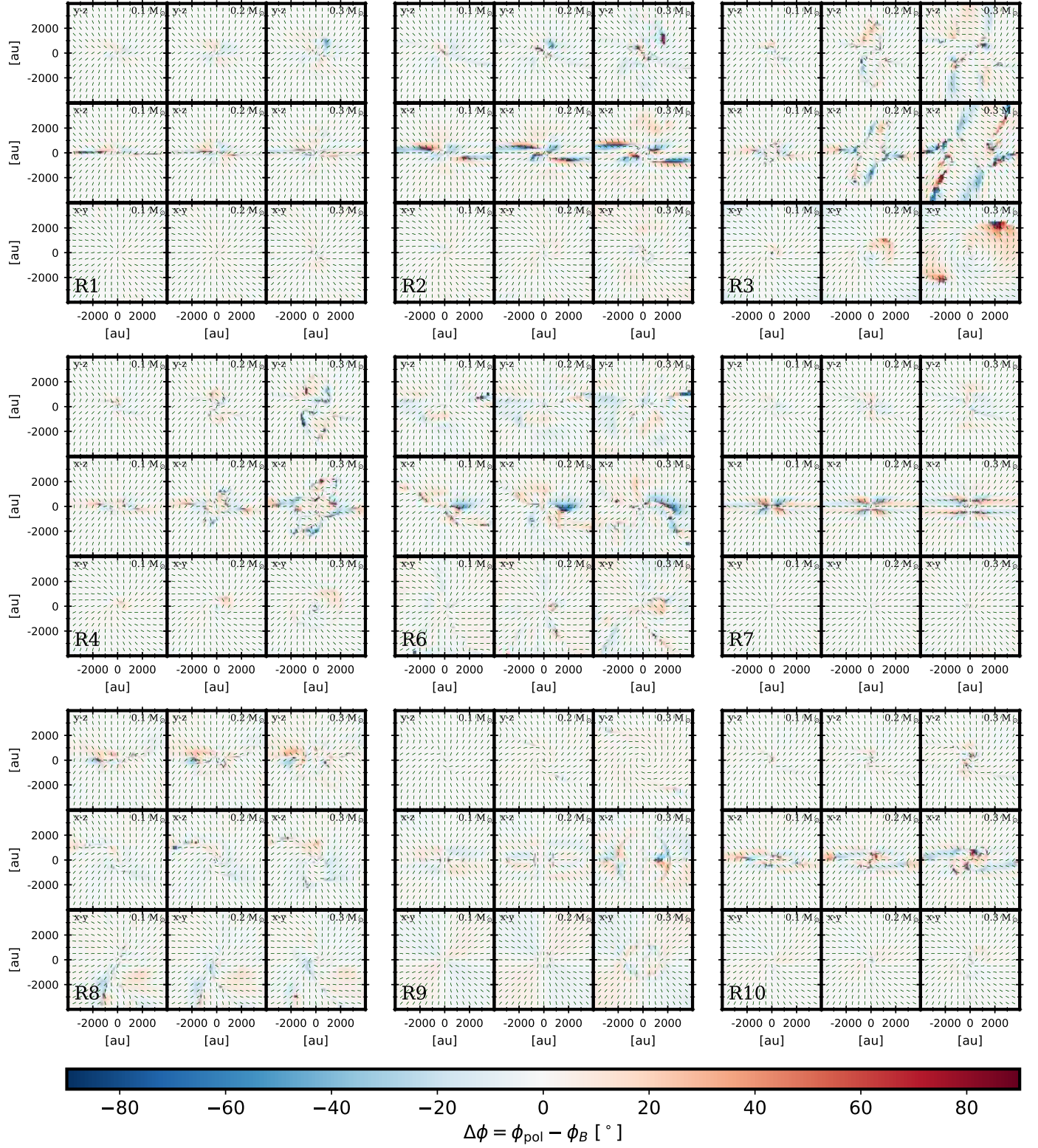


Fig. A.7. $\Delta\phi$ at $\lambda = 3.0$ mm. The structure of the figure is the same than for Figs. A.5 and A.6.

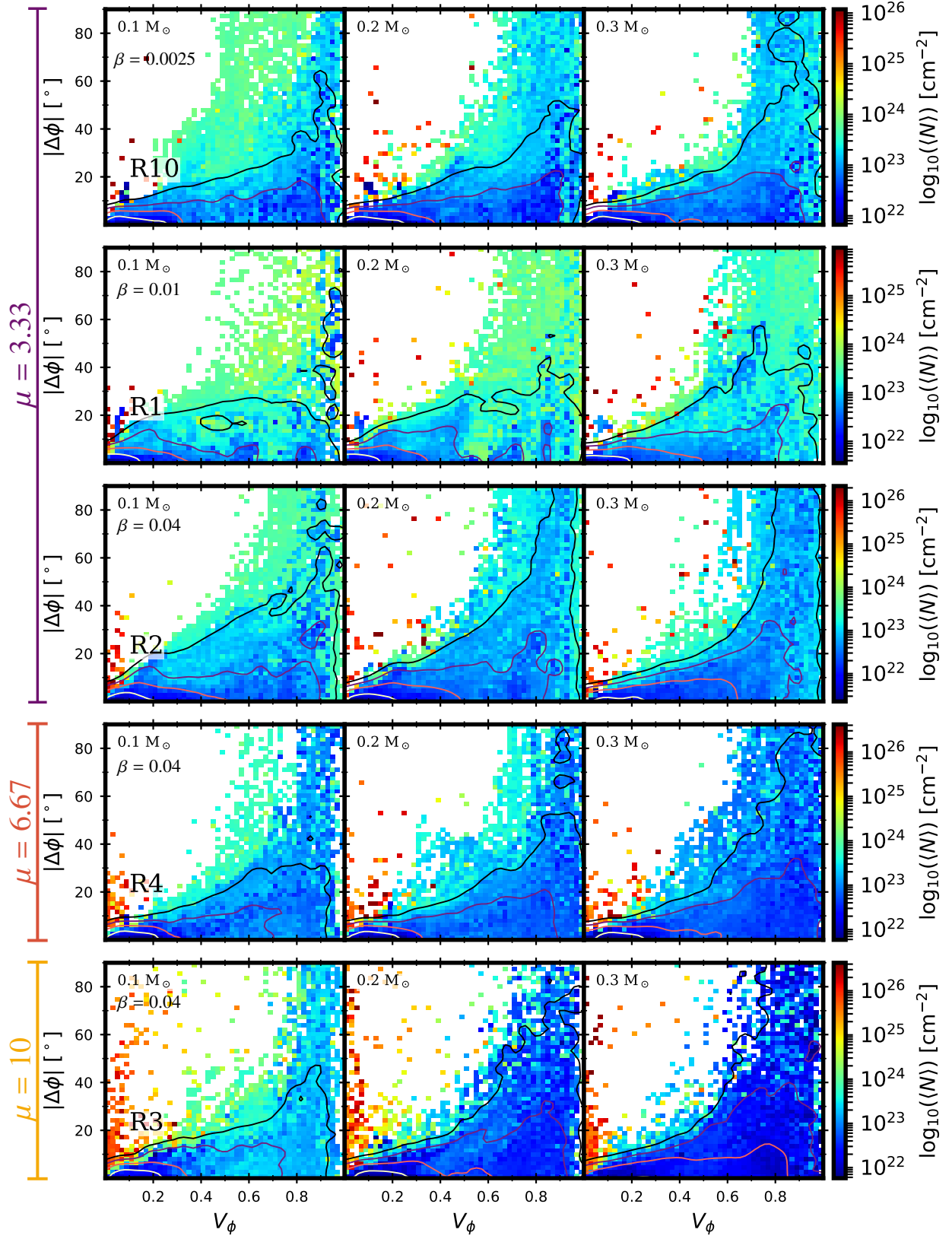


Fig. A.8. Distribution of the discrepancy $|\Delta\phi|$ between the B angle inferred from the synthetic polarized dust emission at $\lambda = 0.8$ mm and the mean orientation of the B lines in the simulation as a function of the circular variance V_ϕ for the simulations with standard conditions. All these simulations do not include any initial turbulence ($M = 0$) and have an initial inclination angle between the initial rotation axis and the magnetic field θ of 30° . The contour lines show the smoothed 2D histogram contour levels at 10^5 (yellow), 10^4 (red), 10^3 (purple), and 10^2 (black) counts. The color coded background corresponds to the mean column density.

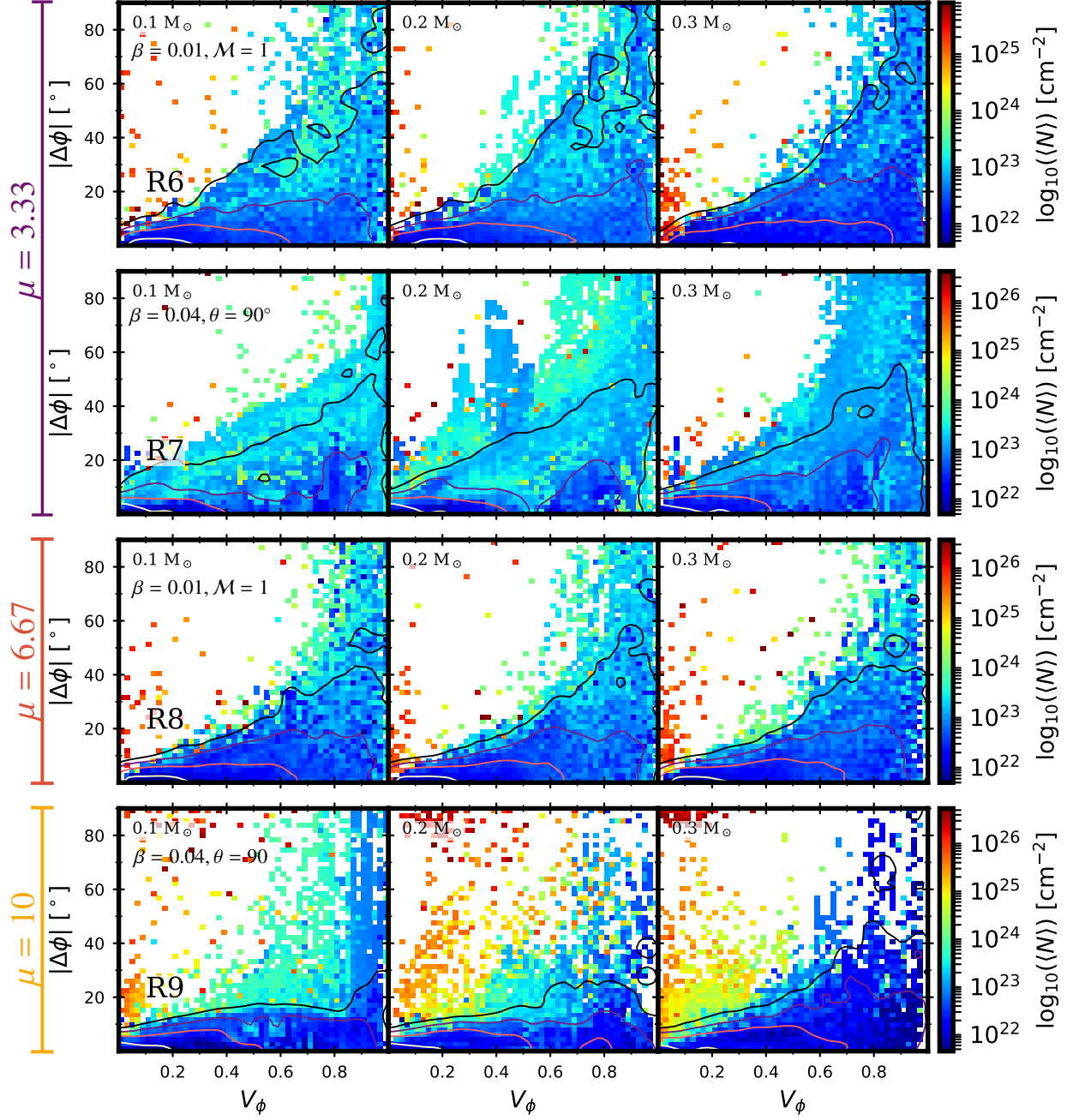


Fig. A.9. Distribution of $|\Delta\phi|$ at $\lambda = 0.8$ mm as a function of the circular variance V_ϕ for the simulations with non standard conditions. The contours and the background image are the same of Fig. A.8. Simulations R6 and R8 include turbulence ($\mathcal{M} = 1$), while the simulations R7 and R9 have an initial angle between the rotation axis and the magnetic field axis of $\theta = 90^\circ$.

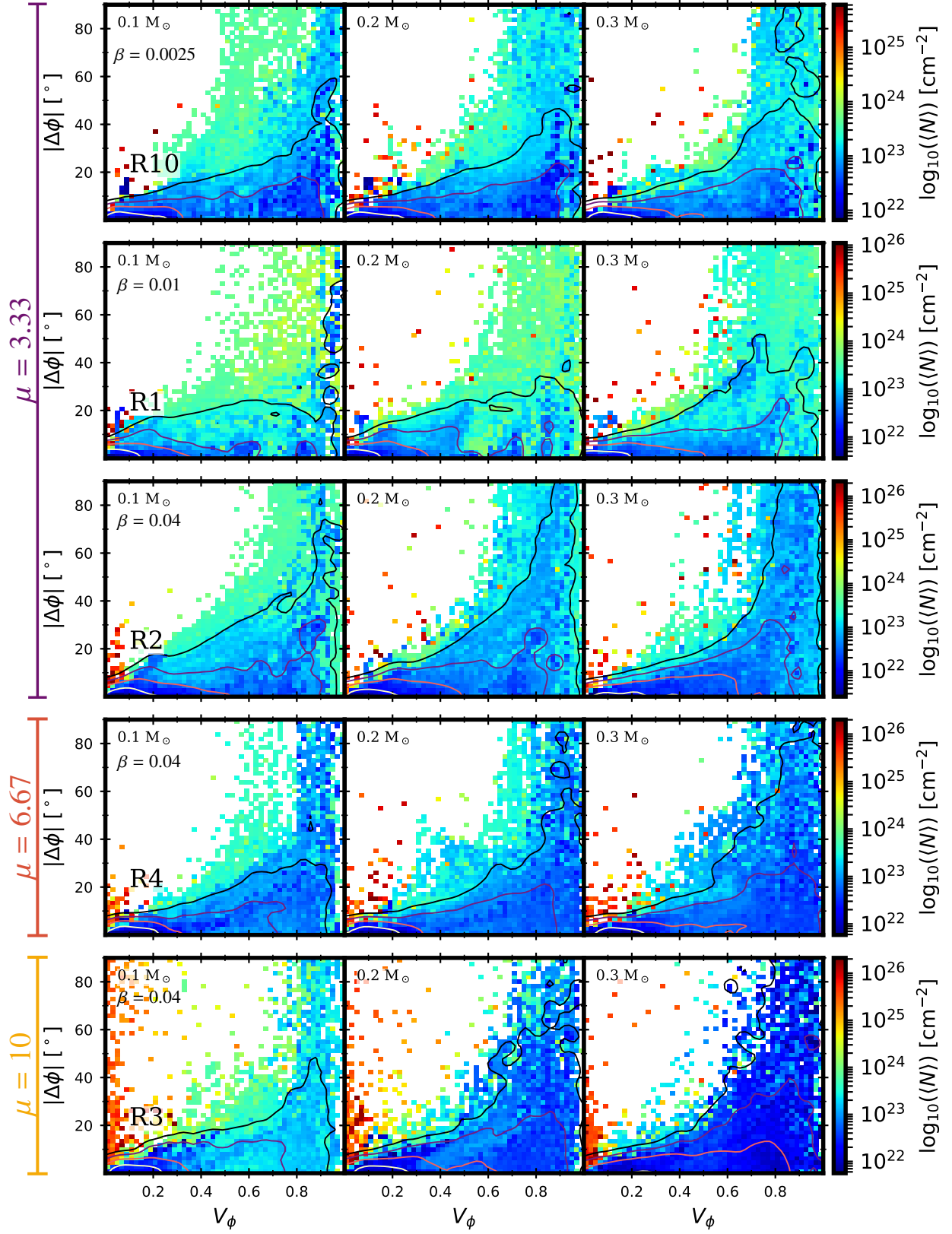


Fig. A.10. Distribution of the discrepancy between the B angle inferred from the synthetic polarized dust emission at $\lambda = 3.0$ mm and the mean orientation of the B lines in the simulation as a function of the circular variance V_ϕ for the simulations with standard conditions. All these simulations do not include any initial turbulence ($M = 0$) and have an initial inclination angle between the initial rotation axis and the magnetic field θ of 30° . The contour lines show the smoothed 2D histogram contour levels at 10^5 (yellow), 10^4 (red), 10^3 (purple), and 10^2 (black) counts. The color coded background corresponds to the mean column density.

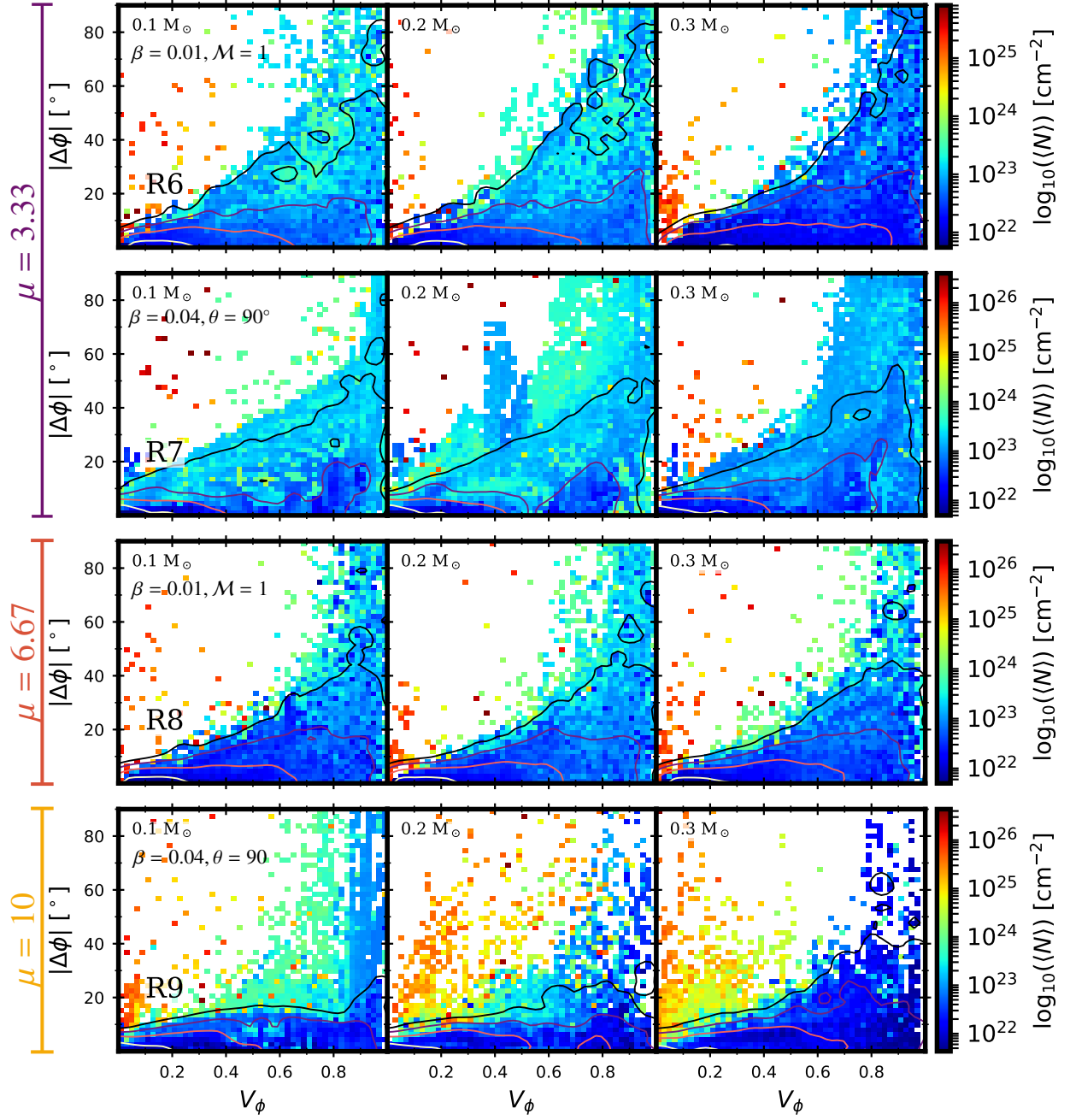


Fig. A.11. Distribution of $|\Delta\phi|$ at $\lambda = 3.0$ mm as a function of the circular variance V_ϕ for the simulations with non standard conditions. The contours and the background image are the same of Fig. A.10. Simulations R6 and R8 include turbulence ($M = 1$), while the simulations R7 and R9 have an initial angle between the rotation axis and the magnetic field axis of $\theta = 90^\circ$.

Table A.1. Fidelity of the B -field mapping from polarized dust emission at $\lambda = 0.8$ mm at different scales.

ID	m_{sink} [M_{\odot}]	los	Recovery rate at different scales [%]				ID	m_{sink} [M_{\odot}]	los	Recovery rate at different scales [%]			
			All scales	30 – 100 au	100 – 500 au	500 – 1500 au				All scales	30 – 100 au	100 – 500 au	500 – 1500 au
R1	0.1	x	99.1	82.2	96.8	99.0	R7	0.1	x	99.3	88.9	96.6	99.5
		y	96.8	60.9	76.3	90.5			y	92.1	55.1	33.6	71.1
		z	>99.9	68.7	>99.9	100.0			z	>99.9	95.1	>99.9	100.0
	0.2	x	97.7	80.5	72.2	95.5		0.2	x	97.8	76.2	70.4	98.6
		y	94.4	66.3	70.3	82.3			y	91.9	93.4	46.1	66.1
		z	>99.9	73.4	99.0	100.0			z	>99.9	92.7	99.5	100.0
	0.3	x	97.2	72.1	90.4	87.0		0.3	x	95.8	76.0	83.6	92.4
		y	93.3	61.5	76.0	84.4			y	89.4	76.6	66.8	63.1
		z	99.5	72.5	90.3	99.5			z	99.8	81.6	96.3	>99.9
R2	0.1	x	97.7	51.0	75.2	97.2	R8	0.1	x	94.8	80.4	70.9	88.0
		y	91.0	50.3	57.0	76.2			y	97.4	70.8	96.6	96.9
		z	99.8	75.7	99.4	>99.9			z	93.2	75.3	90.8	96.6
	0.2	x	96.5	67.2	65.7	86.9		0.2	x	93.5	72.7	79.9	86.5
		y	88.1	79.3	48.4	68.5			y	96.9	78.3	88.5	97.8
		z	99.7	82.8	96.2	99.1			z	93.9	92.0	83.7	95.6
	0.3	x	92.6	69.5	73.8	85.1		0.3	x	92.5	86.8	95.6	87.3
		y	83.7	81.7	79.7	69.6			y	94.7	85.7	87.7	88.7
		z	98.4	67.4	87.1	97.8			z	95.5	85.1	92.2	92.7
R3	0.1	x	98.7	89.4	87.8	94.3	R9	0.1	x	99.8	91.8	99.7	99.5
		y	96.4	93.0	89.7	86.2			y	94.9	97.2	71.4	98.0
		z	98.2	80.2	95.2	99.2			z	99.8	80.7	95.5	100.0
	0.2	x	94.5	86.5	92.8	87.4		0.2	x	99.5	63.7	99.7	98.7
		y	90.5	92.9	97.6	78.7			y	97.1	91.1	91.9	95.1
		z	95.4	77.1	91.1	86.9			z	99.3	79.7	94.9	97.2
	0.3	x	88.7	68.9	96.0	89.1		0.3	x	99.0	67.5	98.5	>99.9
		y	79.7	84.3	97.9	94.6			y	84.4	91.4	90.5	90.0
		z	81.1	67.3	87.6	91.4			z	96.3	90.4	89.4	87.1
R4	0.1	x	98.9	81.7	73.9	96.4	R10	0.1	x	99.3	54.7	84.5	99.2
		y	96.1	86.8	78.1	90.6			y	93.1	82.1	62.1	86.3
		z	99.6	77.2	86.9	99.3			z	99.9	78.0	98.5	99.9
	0.2	x	96.9	69.5	80.1	86.0		0.2	x	98.9	69.6	80.6	97.3
		y	92.7	73.4	87.1	75.6			y	91.6	79.0	46.2	83.7
		z	98.8	74.9	97.3	99.7			z	99.7	59.4	94.5	100.0
	0.3	x	93.0	64.6	70.4	84.0		0.3	x	97.1	61.4	65.5	90.3
		y	85.8	47.8	73.0	73.7			y	89.1	90.4	44.4	65.2
		z	97.1	62.5	88.6	96.0			z	99.0	49.8	84.7	98.6
R6	0.1	x	95.5	81.9	91.5	96.0							
		y	92.5	49.5	74.2	80.0							
		z	96.8	76.7	89.3	98.4							
	0.2	x	93.6	74.8	89.9	97.5							
		y	87.1	50.5	66.3	68.3							
		z	96.8	68.9	91.7	94.1							
	0.3	x	89.5	89.5	82.0	93.2							
		y	83.4	73.1	67.7	78.7							
		z	91.9	71.5	85.1	84.0							

Notes. Here we present the recovery rates obtained for each simulation (ID), evolutionary stage (m_{sink}) and projection (los) using the synthetic observations at $\lambda = 0.8$ mm. The fourth column shows the recovery rate over the whole map, while the rest of the scales correspond to the lines of sight with radial distances to the central source comprised in the interval indicated in the header. A synthesis of this table is given in Table 3.

Table A.2. Influence of the turbulence on the mean fidelity of B -field mapping from polarized dust emission at $\lambda = 0.8$ mm in protostellar envelopes at different scales.

m_{sink} [M_{\odot}]	B -field recovery rates and σ [%]							
	All scales		30 – 100 au		100 – 500 au		500 – 1500 au	
R1	97.5	2.4	70.9	7.5	85.7	12.0	93.1	7.2
R6	91.9	4.5	70.7	13.2	82.0	10.1	87.8	10.5

Notes. Mean recovery rates at different scales for an error bar of 15° . The values have been averaged for all the evolutionary stages and projections for simulations R1 (non-turbulent) and R6 (turbulent) given in Table A.1. The values given in a smaller font correspond to the standard deviation.

Table A.3. Fidelity of B -field mapping from polarized dust emission in protostellar envelopes at $\lambda = 1.3$ mm.

m_{sink} [M_{\odot}]	B -field recovery rates and σ [%]							
	All scales		30 – 100 au		100 – 500 au		500 – 1500 au	
$\mu = 3.33$								
0.1	97.1	3.0	71.9	14.9	83.7	18.4	93.4	9.1
0.2	95.9	4.0	76.2	11.3	77.3	17.9	90.2	11.5
0.3	93.7	5.1	74.6	10.4	79.4	12.5	86.9	11.5
$\mu = 6.67, 10.$								
0.1	97.5	2.0	85.6	7.8	87.9	9.1	95.7	4.4
0.2	96.0	2.7	82.2	9.5	91.3	6.0	90.6	7.1
0.3	91.2	5.8	77.8	13.7	90.7	7.4	90.6	6.5

Notes. Mean recovery rates as in Table 3, but for maps at $\lambda = 1.3$ mm.

Table A.4. Fidelity of B -field mapping from polarized dust emission in protostellar envelopes at $\lambda = 3.0$ mm.

m_{sink} [M_{\odot}]	B -field recovery rates and σ [%]							
	All scales		30 – 100 au		100 – 500 au		500 – 1500 au	
$\mu = 3.33$								
0.1	97.2	3.0	72.9	14.7	84.9	18.0	93.9	8.8
0.2	96.2	3.8	77.4	11.3	78.8	17.3	90.9	11.0
0.3	94.0	5.0	75.8	10.5	80.5	12.0	87.7	11.2
$\mu = 6.67, 10.$								
0.1	97.6	2.0	86.4	7.9	89.1	8.4	95.9	4.3
0.2	96.2	2.7	83.4	10.0	92.1	5.6	91.3	7.1
0.3	91.7	5.6	79.3	13.6	92.2	6.4	91.3	6.4

Notes. Mean recovery rates as in Table 3, but for maps at $\lambda = 3.0$ mm.

Appendix B: Additional tests for understanding the origin of points with low dispersion and high discrepancy

Even though the great majority of discrepancies between the polarization vectors and the mean orientation of the magnetic field can be understood as a consequence of the intrinsic organization level, some points of high discrepancy ($|\Delta\phi| > 30^\circ$) and low disorganization levels ($V_\phi < 0.5$) remain unexplained. To better understand this issue we explore the effect of the opacity, which can cause a signal to be dominated by the foreground external layers, and thus not tracing the full line of sight, and the effect of the alignment efficiency, which if lowered can hinder the ability of polarization to properly trace the magnetic field.

The opacity effect can be studied by analyzing the distribution of $|\Delta\phi|$ as a function of the opacity and the projected radius at the available wavelengths. In Fig. B.1 we present the stacked (for all simulations, projections and timesteps) distribution of the discrepancy $|\Delta\phi|$ as a function of the intrinsic level of disorganization of the field lines (V_ϕ), the opacity (τ) and as a function of the radial distance (r). The colored region corresponds to the subset of points where $|\Delta\phi| > 30^\circ$ and $V_\phi \leq 0.5$, while the grey background corresponds to all the points (given for reference). This figure shows that the bulk of the points at $|\Delta\phi| \sim 30 - 40^\circ$ is still consistent with the intrinsic disorganization level ($\sigma_\phi \sim 30^\circ$ when $V_\phi \sim 0.5$), and that they are likely produced in regions disturbed by the outflows at a distance of 200 – 1000 au. Lines of sight with extremely high discrepancy levels $|\Delta\phi| > 70^\circ$ are associated to regions located within a radius of roughly 100 au with high opacities of about 2 – 100. This might indicate that in these regions the signal recovered in the synthetic observations is just partial. This is coherent with the decrease of the number of problematic lines of sight for longer wavelengths, that have a lower optical depth.

To test the effect of the alignment efficiency we perform an extra set of identical synthetic observations, except for the alignment properties. The POLARIS code allows us to simulate the polarized dust emission arising from perfectly aligned dust grains. When this hypothesis is used, all the dust grains susceptible to be aligned will contribute to the polarized dust emission, and the resulting polarized intensity and polarization fraction will correspond to the upper limits of these quantities. Figure B.2 displays the same plots as Fig. B.1, but for the perfectly aligned dust grains hypothesis. From this figure we find that the number of lines of sight in the region $|\Delta\phi| > 30^\circ$ and $V_\phi < 0.5$ is reduced by 25, 22, and 25% at $\lambda = 0.8, 1.3$, and 3.0 mm, respectively, when using the perfect alignment hypothesis, indicating that a lower alignment efficiency is also contributing to a worse description of the mean magnetic field orientation, especially in the inner 200 au. Additionally, these results highlight the role of the opacity effects, since even though dust grains are perfectly aligned, there are remaining patches of problematic lines-of-sight. This is likely due to the fact that the emission is dominated by the most external layers in the foreground, which is consistent with the fact that the number of conflicting lines of sight decreases with the observed wavelength (or equivalently with the opacity).

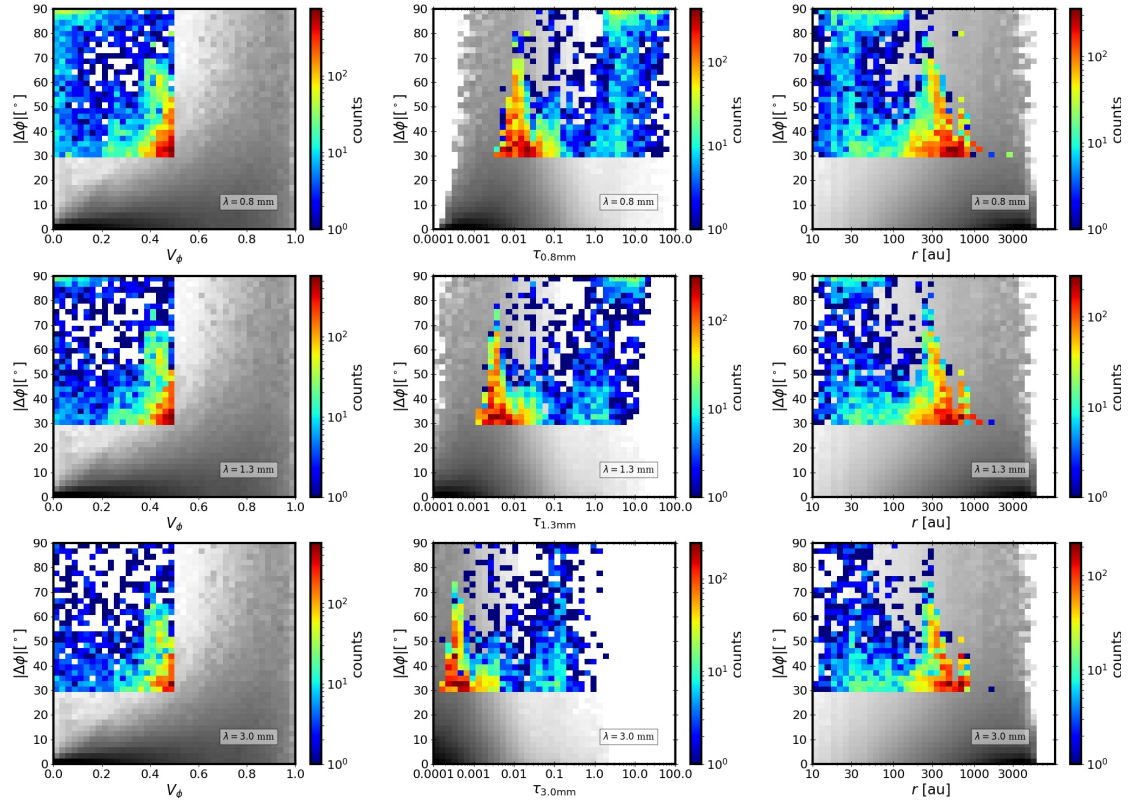


Fig. B.1. 2D histograms for the RAT case of the stacked maps (all simulations, timesteps, and projections) showing the $\Delta\phi$ as a function of V_ϕ , vs optical depth and vs the radial distance r (from left to right), at three wavelengths $\lambda = 0.8, 1.3, 3.0$ mm (top to bottom).

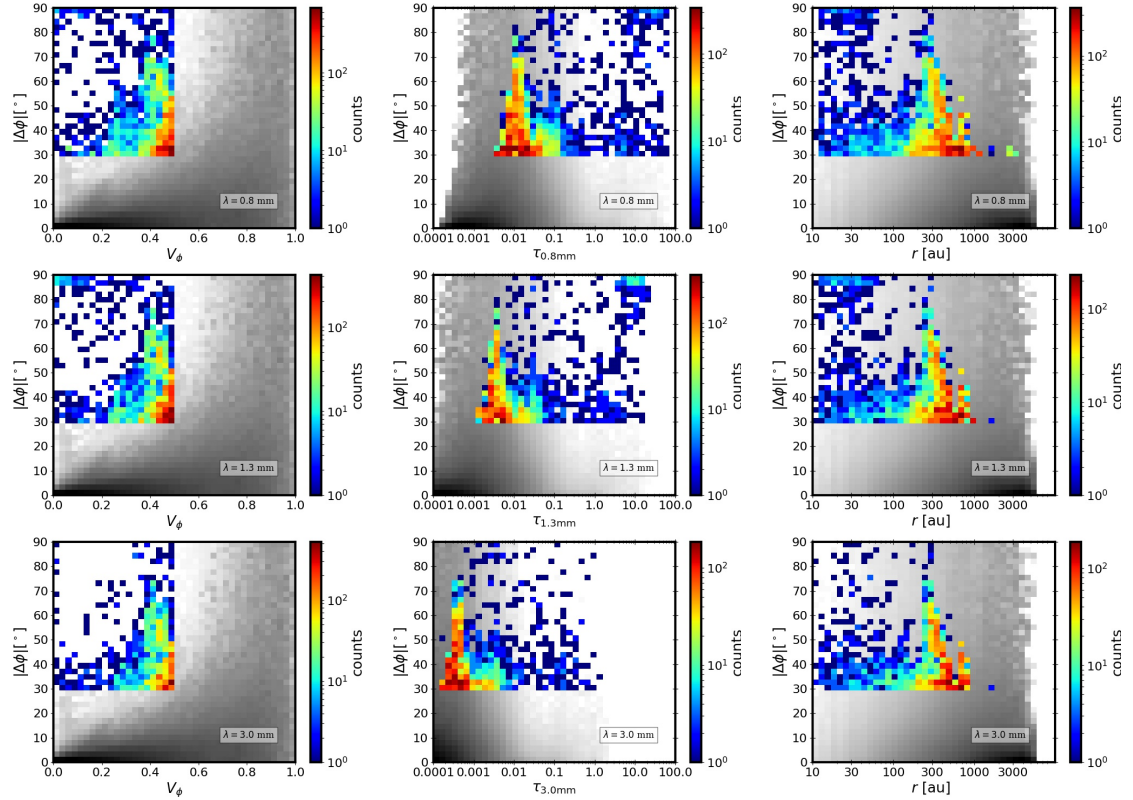


Fig. B.2. The same as Fig. B.1, but for the case where dust grains are perfectly aligned.

Appendix C: Relation between the circular variance and the angular dispersion

To understand how the circular variance (V_ϕ), defined in Sect. 2.3, and the angular dispersion (σ_ϕ) are related we simulate several ensembles of random angles and we compute the resulting V_ϕ and σ_ϕ . To avoid any bias related to the position angle, we set 180 regularly spaced central angles (ϕ_c) from -90° to 89° . Secondly, around each central angle we define 18 opening angles $\Delta\theta$, varying from 5° to 90° and we randomly generate an ensemble of $N = 500$ uniformly distributed angles in the interval $[\phi_c - \Delta\theta, \phi_c + \Delta\theta]$.

Since the mean angle does not represent the true orientation when dealing with bidirectional data, we define the mean orientation $\langle\phi\rangle$ as in Eq 3. The dispersion is thus defined as follows:

$$\sigma_\phi = \sqrt{\frac{1}{N} \sum_{i=1}^N (\phi_i - \langle\phi\rangle)^2}, \quad (\text{C.1})$$

where we use the smallest difference with respect to the mean mean orientation ($|\phi_i - \langle\phi\rangle| \leq 90^\circ$).

We compute V_ϕ and σ_ϕ for each ensemble, and we repeat the procedure 200 times for each central angle and opening angle (totaling 648000 ensembles). We present the results for the relation between the circular variance V_ϕ and the angular dispersion in Fig. C.1. Each point of the figure show the circular variance as a function of the angular dispersion of each individual simulated ensemble of 500 data points. In this figure we have color coded the opening angle $\Delta\theta$ of each ensemble. Note that the angular dispersion is necessarily smaller than $\Delta\theta$, which only represents the maximum allowed variation with respect to the central angle

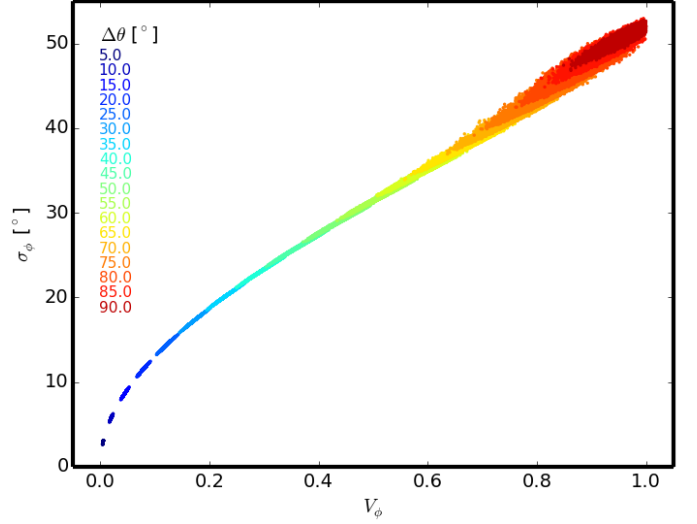


Fig. C.1. Relation between the circular variance V_ϕ and the angular dispersion.

ϕ_c .

Figure C.1 shows that σ_ϕ increases monotonically with V_ϕ (and with $\Delta\theta$), but its maximum value is limited to less than 55° .